



**UNIVERSIDAD DE INVESTIGACIÓN DE TECNOLOGÍA  
EXPERIMENTAL YACHAY**

**Escuela de Ciencias Físicas y Nanotecnología**

**TÍTULO: Photoconductive Behavior and Structural Analysis of  
Copper Oxide Nanocomposites Embedded in Chitosan Films.**

Trabajo de integración curricular presentado como requisito  
para la obtención del título de Ingeniero en Nanotecnología

**Autor:**

Minango Freire Jhoao Fernando

**Tutor:**

PhD. Bramer Escamilla Werner

**Co-Tutor:**

PhD. Gonzalez Vasquez Gema

Urququí - Enero 2025

## **Autoría**

Yo, **Minango Freire Jhoao Fernando**, con cedula de identidad **1723435531**, declaro que las ideas, juicios, valoraciones, interpretaciones, consultas bibliográficas, definiciones y conceptualizaciones expuestas en el presente trabajo; así cómo, los procedimientos y herramientas utilizadas en la investigación, son de absoluta responsabilidad de el autor del trabajo de integracion curricular. Así mismo, me acojo a los reglamentos internos de la Universidad de Investigación de Tecnología Experimental Yachay.

Urcuquí, Enero 2025

---

Jhoao Fernando Minango Freire  
CI: 1723435531

## **Autorizacion de publicación**

Yo, **Minango Freire Jhoao Fernando**, con cedula de identidad **1723435531**, cedo a la Universidad de Investigación de Tecnología Experimental Yachay, los derechos de publicación de la presente obra, sin que deba haber un reconocimiento económico por este concepto. Declaro además que el texto del presente trabajo de titulación no podrá ser cedido a ninguna empresa editorial para su publicación u otros fines, sin contar previamente con la autorización escrita de la Universidad.

Asimismo, autorizo a la Universidad que realice la digitalización y publicación de este trabajo de integración curricular en el repositorio virtual, de conformidad a lo dispuesto en el Art. 144 de la Ley Orgánica de Educación Superior.

Urcuquí, Enero 2025

---

Jhoao Fernando Minango Freire

CI: 1723435531



## **Dedication**

For all the people that trust in me. I hope that better times coming soon.

Jhoao Fernando Minango Freire



## **Acknowledgements**

To my family, the principal reason to do this. To my friends Ari, Abi, Nath, Jury, Damian, Lenin, Martina, Mabel, Bruna and the other people who made my pass for this period of my life an awesome experience. To my mom and dad for support all these years with my far away of home. To my sister Vane, for be my confident. I hope that the way that I suffer, it wanna be more easier for you now that I have the complete college experience. To my professors, specially to my tutors, that open me the doors of a new world in science. To Ana, you were this surprise that I appreciate for the rest of my life. I do not have enough words to express all the feelings that this work have. Thanks

Jhoao Fernando Minango Freire

## Resumen

El presente trabajo de investigación se centra en el desarrollo de dispositivos optoelectrónicos utilizando tecnología de semiconductores extrínsecos, específicamente empleando una matriz de quitosano incrustada con nanopartículas de óxido de cobre (I) y óxido de cobre (II) ( $Cu_2O$  y  $CuO$ ). La síntesis de estos dispositivos de fotoconductancia implica la fabricación de nanocompuestos, donde las nanopartículas de óxido de cobre se dispersan uniformemente dentro de la matriz polimérica de quitosano. Este proceso incluye un control preciso del tamaño y la composición de las nanopartículas mediante tratamientos térmicos a diferentes temperaturas, con el fin de optimizar las propiedades de las películas resultantes.

Las propiedades ópticas y estructurales de los nanocompuestos se caracterizaron utilizando espectroscopía UV-Vis y difracción de rayos X (XRD), revelando fases distintas de  $Cu_2O$  y  $CuO$  dependiendo de la temperatura de calcinación. Se observó que el tamaño de las partículas aumenta con mayores temperaturas de calcinación, afectando los valores de la brecha de banda y las propiedades de absorción óptica de las películas. La fotoconductancia de las películas se midió utilizando un sistema de adquisición de datos (DAQ) diseñado específicamente, el cual demostró que las muestras calcinadas a temperaturas más altas (600 °C) exhibieron mejor fotoconductancia que aquellas calcinadas a temperaturas más bajas (350 °C).

Además, el uso de filtros de luz (rojo, verde y azul) permitió un análisis detallado de cómo diferentes longitudes de onda afectan la respuesta fotoconductiva de los nanocompuestos. Los resultados indican que la fotoconductancia de las películas es altamente sensible al proceso de calcinación y la composición específica de los óxidos de cobre, lo que hace que estos materiales sean candidatos adecuados para aplicaciones en dispositivos optoelectrónicos, especialmente en entornos donde la absorción de luz controlada y la fotoconductancia son cruciales.

Esta investigación resalta la importancia de optimizar los procesos de síntesis y tratamiento térmico para ajustar las propiedades electrónicas de las nanopartículas de óxido de cobre incrustadas en una matriz polimérica biocompatible, demostrando su potencial en aplicaciones optoelectrónicas sostenibles.

**Palabras clave:** nanocompuestos, dispositivos optoelectrónicos, óxido de cobre, quitosano, fotoconductancia, tratamiento térmico.



## Abstract

The present research focuses on the development of optoelectronic devices using extrinsic semiconductor technology, specifically employing a chitosan matrix embedded with copper (I) and copper (II) oxide nanoparticles ( $Cu_2O$  and  $CuO$ ). The synthesis of these photoconductance devices involves the fabrication of nanocomposites, where copper oxide nanoparticles are uniformly dispersed within the chitosan polymer matrix. This process includes precise control over nanoparticle size and composition through thermal treatments at different temperatures to optimize the properties of the resulting films.

The optical and structural properties of the nanocomposites were characterized using UV-Vis spectroscopy and X-ray diffraction (XRD), revealing distinct phases of  $Cu_2O$  and  $CuO$  depending on the calcination temperature. The particle size was found to increase with higher calcination temperatures, affecting the bandgap values and optical absorption properties of the films. The photoconductance of the films was measured using a custom-built data acquisition (DAQ) system, which demonstrated that samples calcinated at higher temperatures (600 °C) exhibited better photoconductance than those calcinated at lower temperatures (350 °C).

Additionally, the use of light filters (red, green, and blue) allowed for an in-depth analysis of how different wavelengths affect the photoconductive response of the nanocomposites. The results indicate that the photoconductance of the films is highly sensitive to the calcination process and the specific composition of the copper oxides, making these materials suitable candidates for applications in optoelectronic devices, particularly in environments where controlled light absorption and photoconductance are crucial.

This research highlights the importance of optimizing the synthesis and thermal treatment processes to tailor the electronic properties of copper oxide nanoparticles embedded in a biocompatible polymer matrix, demonstrating their potential in sustainable optoelectronic applications.

**Keywords:** nanocomposites, optoelectronic devices, copper oxide, chitosan, photoconductance, thermal treatment.



# Contents

|          |   |           |
|----------|---|-----------|
| <b>1</b> | <b>Introduction</b>   | <b>1</b>  |
| 1.1      | Problem Statement . . . . .   | 2         |
| 1.2      | Objectives . . . . .  | 2         |
| 1.2.1    | General objective . . . . .   | 2         |
| 1.2.2    | Specific objectives . . . . .   | 2         |
| <b>2</b> | <b>Theoretical framework</b>  | <b>3</b>  |
| 2.1      | Nanocomposites . . . . .  | 4         |
| 2.2      | Optoelectronic devices . . . . .                                      | 5         |
| 2.3      | Semiconductors based on Nanoparticles . . . . .                       | 5         |
| <b>3</b> | <b>Methodology</b>  | <b>7</b>  |
| 3.1      | Materials and Equipment . . . . .                                     | 7         |
| 3.1.1    | Synthesis of $Cu_2O$ and $CuO$ NPs . . . . .                          | 7         |
| 3.1.2    | Interdigitates Elaboration . . . . .                                  | 9         |
| 3.1.3    | Chitosan $Cu_2O/CuO/Cu^+$ and $CuO/Cu_2O$ films fabrication . . . . . | 10        |
| 3.1.4    | Equipment used to characterized . . . . .                             | 10        |
| 3.2      | DAQ "NI USB-6210" Circuit . . . . .                                   | 11        |
| <b>4</b> | <b>Results</b>  | <b>13</b> |
| 4.1      | XRD . . . . .   | 13        |
| 4.2      | UV-Vis Spectroscopy . . . . .   | 17        |
| 4.3      | Chitosan Films elaboration . . . . .                                  | 23        |
| 4.4      | DAQ "NI USB-6210" Circuit . . . . .                                   | 26        |
| <b>5</b> | <b>Conclusions</b>  | <b>35</b> |
|          | <b>Bibliography</b>   | <b>37</b> |
|          | <b>Appendices</b>   | <b>40</b> |



# List of Figures

|      |  |    |
|------|--|----|
| 2.1  | Preparation methods for nanocomposites: (a) melt compounding, (b) film casting <sup>11</sup> . . . . .   | 5  |
| 3.1  | Chemical elaboration of copper NPs process. . . . .  | 8  |
| 3.2  | Interdigitated fabrication process. The process includes the design, cleaning, pattern transfer, and chemical etching to obtain the interdigitated pattern on the copper plate. . . . .  | 9  |
| 3.3  | Fabrication process of chitosan films with copper oxide nanoparticles. The process involves the preparation of a chitosan solution, incorporation of nanoparticles, and application on the interdigitated electrodes, followed by drying under sunlight. . . . .   | 10 |
| 3.4  | Rigaku MiniFlex 600 X-ray Diffractometer taking the measure of the first synthesis sample . . . . .  | 11 |
| 3.5  | DAQ Circuit Diagram . . . . .  | 12 |
| 4.1  | X-ray diffraction (XRD) pattern of the first synthesized sample, showing the characteristic peaks corresponding to $Cu^+$ , $Cu_2O$ , and $CuO$ phases. The analysis provides insight into the structural composition and phase purity of the nanoparticles. . . . .   | 13 |
| 4.2  | X-ray diffraction (XRD) analysis of the sample calcinated at $350^{\circ}C$ for one hour. This figure reveals the emergence of $Cu_2O$ and $CuO$ phases, with reduced intensity of $Cu^+$ peaks, demonstrating the effect of thermal treatment on the nanoparticle structure. . . . .                            | 14 |
| 4.3  | XRD $600^{\circ} C$ for 1 hour sample . . . . .  | 15 |
| 4.4  | XRD comparison of $350$ and $600^{\circ} C$ calcinated samples . . . . .   | 16 |
| 4.5  | Absorption vs Wavelength UV-Vis spectrum comparison between samples . . . . .  | 17 |
| 4.6  | Tauc Plot Comparison between samples recognized the first bandgap of each sample. . . . .  | 18 |
| 4.7  | Tauc Plot Comparison between samples recognized the second bandgap of each sample. . . . .   | 19 |
| 4.8  | Tauc Plot of $350^{\circ}C$ calcinated sample . . . . .  | 19 |
| 4.9  | First Band Gap recognized in Tauc Plot of $350^{\circ}C$ . . . . .   | 20 |
| 4.10 | UV-vis spectrum with the inset is the Tauc plot pattern of a $Cu_2O$ NPs sample recover from (Zayed. M. F. 2020) <sup>30</sup> . . . . .   | 20 |
| 4.11 | Second Band Gap recognized in Tauc Plot of $350^{\circ}C$ . . . . .  | 21 |
| 4.12 | Tauc Plot of $600^{\circ}C$ sample . . . . .   | 21 |
| 4.13 | First Band Gap recognized in Tauc Plot of $600^{\circ}C$ . . . . .   | 22 |
| 4.14 | Second Band Gap recognized in Tauc Plot of $600^{\circ}C$ . . . . .  | 23 |
| 4.15 | Corrosion produced by lack of sunlight . . . . .   | 24 |
| 4.16 | Color comparison of the [chitosan/ $350^{\circ}C$ ] sample before and after ultrasound treatment. The left image shows the sample's dark coloration before treatment, while the right image shows the brick-like matte color after ultrasound treatment, indicating possible nanoparticle agglomeration. . . . . | 24 |

|      |  |    |
|------|--|----|
| 4.17 | Comparative between 600 and 350 ° C calcinated samples after ultrasound treatment. . . . .   | 25 |
| 4.18 | New Chitosan/350 °C sample (left) prepared in compare with an old Chitosan/350 °C sample (right) . . .   | 25 |
| 4.19 | DAQ "NI USB-6210" Circuit Set Up . . . . .   | 26 |
| 4.20 | RC Series Circuit showing the charge and discharge behavior of a capacitor. The graph illustrates the voltage across the capacitor (VC) and the input voltage (V0) over time. Recover from (PASCO Scientific, 2024) . . . . .  | 27 |
| 4.21 | Blank Control recover from [Chitosan/600°C] sample at 1% NPs, recorded using the DAQ 'NI USB-6210' Circuit. . . . .  | 28 |
| 4.22 | Current measurement of the [Chitosan/600°C] sample at 1% NPs, recorded using the DAQ 'NI USB-6210' Circuit. This graph illustrates the photoconductive behavior under white light exposure, showing a stable response similar to a capacitor with an average amplitude of 0.075 $\mu$ A. . . . . | 28 |
| 4.23 | Compare between control measure and white light measure of 600 °C at 1% NPs concentration interdigitate.   | 29 |
| 4.24 | Light Filters spectrums employed in analysis in photoconductance of [Chitosan/600 °C] at 1% NPs. . . .   | 29 |
| 4.25 | Interdigitate under a blue light filter current measure . . . . .  | 30 |
| 4.26 | Compare between a control measure and blue filter measure. . . . .   | 31 |
| 4.27 | Compare between a control measure and green filter measure. . . . .  | 31 |
| 4.28 | Interdigitate under a green light filter current measure . . . . .   | 32 |
| 4.29 | Interdigitate under a red light filter current measure . . . . .   | 33 |
| 4.30 | Compare between control measure and red filter . . . . .   | 34 |
| 1    | AFM height forward measure of first synthesis of metallic copper oxide NPs . . . . .   | 43 |

# Chapter 1

## Introduction

Currently, the semiconductor industry is one of the fastest-growing industries in the world, reporting worldwide sales of \$141.13 billion in 2022, only in America<sup>1</sup>. This industry plays an important role in different sectors such as telecommunications, medical electronics, automobile, defense and aerospace, consumer electronics, etc. In addition, the miniaturization of most semiconductors significantly reduces their useful life due to fragility, producing a lot of electronic waste year after year<sup>2</sup>. In contrast, new research focuses on the implementation of new materials aligned with the values of green chemistry. Metallic oxide nanoparticles such as  $Cu_2O$ ,  $CuO$ ,  $ZnO$ ,  $Ag_2O$ , and  $TiO_2$  in an organic matrix show photovoltaic behavior that can be employed in the development of new semiconductors with chemical and physical advantages, such as improved mechanical properties and increased energy efficiency<sup>3</sup>.

In optoelectronic devices, the application of metallic nanoparticles have garnered significant attention due to their unique physical and chemical properties. Copper oxide nanoparticles, in particular, stand out for their versatile applications in areas such as catalysis, energy conversion, and environmental remediation<sup>4</sup>. This thesis explores the incorporation of copper oxide nanoparticles ( $CuO$  and  $Cu_2O$ ) within a chitosan matrix, aiming to harness their potential in optoelectronic devices and biodegradable materials. The choice of chitosan, a biocompatible and environmentally friendly biopolymer, as a host matrix, offers a promising pathway to enhance the functional attributes of copper oxide nanoparticles while adhering to the principles of green chemistry and sustainability<sup>5</sup>.

Interest in copper oxide nanoparticles, specifically those of copper(I) oxide ( $Cu_2O$ ) and copper(II) oxide ( $CuO$ ), characterized by their precise size and shape, stems from their advantageous optical and electronic properties. Diverse micro and nanostructures of  $Cu_2O$  have been synthesized by numerous researchers, including nanocubes, octahedra, nanocages, hollow spheres, nanowires, and other highly symmetrical configurations<sup>6</sup>. These nanoparticles are widely recognized materials extensively utilized in the semiconductor industry. Different research indicates their considerable potential as p-type semiconductors with a direct band gap of 2.17 eV, coupled with distinctive optical and magnetic characteristics, ease of accessibility, and low toxicity<sup>7,8</sup>. The robust stability of Cu nanoparticles in ambient air is attributed to the oxidation of metallic copper surfaces into  $Cu_2O$  and  $CuO$ , with the composition of these oxides evolving over exposure time<sup>9</sup>.

The use of inorganic nanoparticles in the polymer matrix can provide a material that presents features such as superparamagnetism, size-dependent band-gap, ferromagnetism, and electron and phonon transport<sup>10</sup>. Chitosan is a natural carbohydrate biopolymer derived by N-deacetylation of chitin that demonstrates the ability to adsorb many metal cations. On the other hand, the systems prepared by immobilization of cations by the chitosan matrix can be considered ecologically friendly catalysts<sup>11</sup>.

The overarching goal of this research is to develop a comprehensive understanding of the interactions between copper oxide nanoparticles and chitosan for optoelectronic properties.

## **1.1 Problem Statement**

Amidst a growing focus on sustainability and efficiency in the semiconductor industry, there is a critical need to develop optoelectronic devices that are not only efficient and high-performing but also aligned with the principles of green chemistry. This study aims to design and synthesize an innovative optoelectronic device using a chitosan matrix combined with copper oxide nanoparticles ( $Cu_2O$  and  $CuO$ ), exploring the synergies between these materials to enhance the optoelectronic properties of the device. The goal is to achieve an optimal balance between optoelectronic efficiency.

## **1.2 Objectives**

### **1.2.1 General objective**

Design thin film composites of copper oxide nanoparticles in chitosan matrix and characterize the photoconductance properties

### **1.2.2 Specific objectives**

1. Synthesis of  $CuO$  and  $Cu_2O$  NPs.
2. Structural and optical Characterization of copper oxides NPs
3. Synthesize chitosan film with different concentration of copper oxide NPs.
4. Measure the photoconductance in function of the percentage of copper oxide NPs in the film.



# Chapter 2

## Theoretical framework

When discussing why semiconductors differ from conductors and insulators, the key factor is their band gap. The concept of the band gap explains how certain materials can facilitate the movement of electrons ( $e^-$ ) between the valence band and the conduction band<sup>12</sup>. The ability to regulate the flow of these electrons forms the foundation of modern electronic technology<sup>13</sup>. Table 2.1 illustrates the typical band gap values of various solid materials, as recovered from Yacobi (2003)<sup>14</sup>. This table is crucial for understanding the fundamental differences between conductors, semiconductors, and insulators. In semiconductors, the band gap represents the energy required for electrons to transition from the valence band to the conduction band, enabling current conduction. Compared to conductors, which either have no band gap or a very small one, semiconductors exhibit a more substantial band gap, allowing for precise control of conductivity through doping and other techniques.

In this research, understanding band gap values is essential, as copper oxide nanoparticles ( $Cu_2O$  and  $CuO$ ) exhibit band gaps that make them well-suited for use in optoelectronic devices.  $Cu_2O$  has a direct band gap of approximately 2.1 eV, allowing it to absorb visible light, while  $CuO$  has a smaller band gap of around 1.2 eV, enabling absorption in the near-infrared spectrum. These properties are critical for the photoconductance behavior of the materials analyzed in this thesis where extrinsic semiconductors works in function of percentage of impurities allow for the control of their conductivity, which is crucial in the fabrication of transistors, solar cells, light-emitting diodes (LEDs), and digital and analog integrated circuits<sup>15</sup>.

Table 2.1: Band gaps of different solid materials recover from (Yacobi. B. G. 2003)<sup>14</sup>

| Material       | Conduction Band                                     | Valence Band   | Energy Gap       |
|----------------|---|--|------------------|
| Insulators     | Empty,<br>large energy gap                          | Fully filled,<br>far from conduction band              | Large gap        |
| Semiconductors | Empty or partially filled,<br>close to valence band | Partially or fully filled,<br>close to conduction band | Small gap        |
| Metals         | Partially filled or overlaps<br>with valence band   | Overlaps with conduction band                          | No gap (overlap) |

In this context, Semiconductors can be divided into two groups: intrinsic and extrinsic. The key difference lies in the presence of intentional impurities, or dopants, throughout the structure of extrinsic semiconductors, which modify their electrical properties. For this reason understanding the differences between them is essential for any study involving semiconductor materials<sup>16</sup>. Next, a table with the principal features is presented as a quickly review:

Table 2.2: Comparison of Intrinsic and Extrinsic Semiconductors<sup>17</sup>

| <b>Characteristic</b>         | <b>Intrinsic Semiconductors</b>  | <b>Extrinsic Semiconductors</b>   |
|-------------------------------|--|---|
| <b>Purity</b>                 | Pure form, no significant impurities.  | Contains intentional impurities.  |
| <b>Charge Carriers</b>        | Charge carriers are generated only by the thermal energy available within the material.                      | Charge carriers introduced (additional electrons or holes).   |
| <b>Conductivity</b>           | Lower conductivity, dependent on temperature to provide energy for electron transition.                      | Higher conductivity at normal temperatures due to additional charge carriers from doping.                         |
| <b>Temperature Dependence</b> | Conductivity increases with temperature as more electrons gain enough energy to jump to the conduction band. | Less temperature-dependent conductivity, as dopants provide charge carriers that require less energy to activate. |
| <b>Applications</b>           | Used in high-precision applications such as high-frequency and high-temperature devices.                     | Fundamental to most electronic devices like diodes, transistors, and integrated circuits.                         |

In this research, our focus is on the development of optoelectronic devices using extrinsic semiconductor technology, specifically incorporating environmentally friendly green chemistry methods<sup>17</sup>. The devices are based on a chitosan film matrix embedded with copper oxide (I) and (II) metallic nanoparticles (NPs). The synthesis of these advanced devices involves the careful preparation of nanocomposites, where the copper oxide nanoparticles are uniformly dispersed within the chitosan polymer matrix<sup>18</sup>. The green chemistry approaches we employ focus on reducing harmful byproducts and waste, using non-toxic solvents and reagents, and improving the overall sustainability of the manufacturing process. These methods are not only better for the environment, but they also often result in more cost-effective manufacturing processes and safer products<sup>19</sup>.

## 2.1 Nanocomposites

Nanocomposites present an attractive alternative for semiconductor fabrication, as illustrated in Fig. 2.1, where two different methods for their preparation can be observed. For this research, the chosen method was film casting. In this method, commonly used host materials include carbonaceous materials like granular activated carbon, silica, cellulose, and polymers. Polymeric materials are particularly notable due to their controllable pore space, mechanical properties, and long useful life<sup>20</sup>.

This matrix not only acts as a supportive scaffold enhancing the mechanical stability of the films but also interacts chemically with the copper oxide nanoparticles, potentially altering their electronic properties and improving the overall photoconductivity of the device<sup>10</sup>.

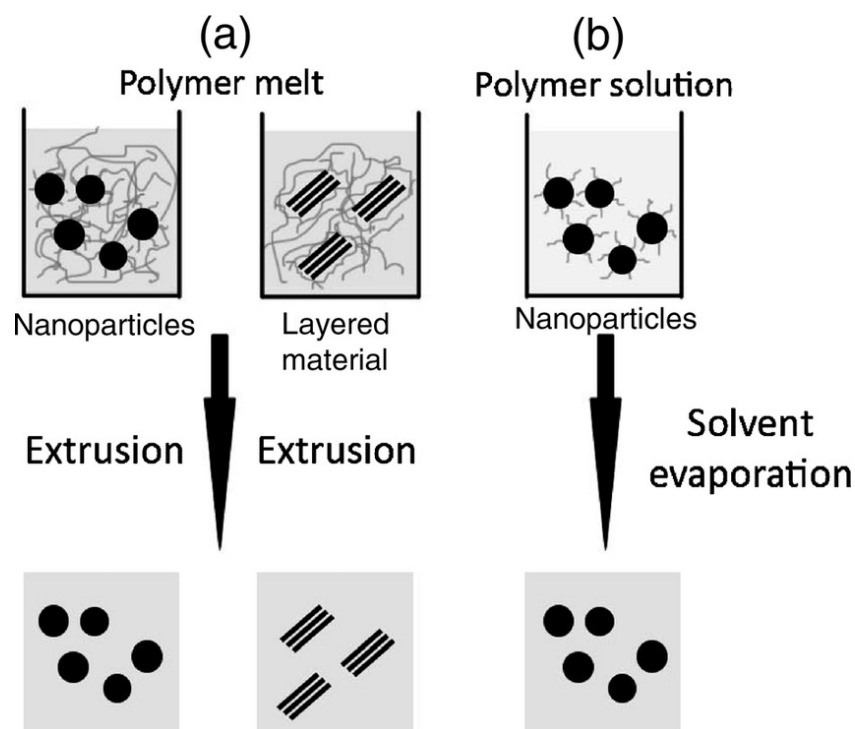


Figure 2.1: Preparation methods for nanocomposites: (a) melt compounding, (b) film casting<sup>11</sup>

## 2.2 Optoelectronic devices

Optoelectronic devices are critical components in modern technology, bridging the gap between optical and electronic systems. These devices include light-emitting diodes (LEDs), photodetectors, and solar cells, which rely on the interaction between light and semiconductor materials to function. The integration of green chemistry principles into the fabrication of optoelectronic devices involves using sustainable materials and processes that minimize environmental impact. For instance, the incorporation of chitosan, a biocompatible and biodegradable polymer, as a matrix for embedding copper oxide nanoparticles, aligns with the goals of reducing hazardous waste and promoting the use of renewable resources. The use of these eco-friendly materials not only enhances the environmental sustainability of the manufacturing process but also often improves the device's overall performance, offering advantages such as increased energy efficiency and enhanced mechanical properties<sup>21,22</sup>.

## 2.3 Semiconductors based on Nanoparticles

A semiconductor nanomaterials constitute a new kind of material that present features as passing current more easily in one direction than the other, showing variable resistance, and sensitivity to light or heat<sup>23</sup>. In this way, metal NPs show an interaction with physical and chemical properties of organic, inorganic, and biomolecules materials<sup>24</sup>.

The dimension of matter that is important to nanoscience and nanotechnology is typically on the 0.2- to 100-nm scale (nanoscale). At this scale, the surface-to-volume ratios of materials become large and their electronic energy states become discrete, leading to unique electronic, optical, magnetic, and mechanical properties of the nanomaterials.



# Chapter 3

## Methodology

### 3.1 Materials and Equipment

#### 3.1.1 Synthesis of $Cu_2O$ and $CuO$ NPs

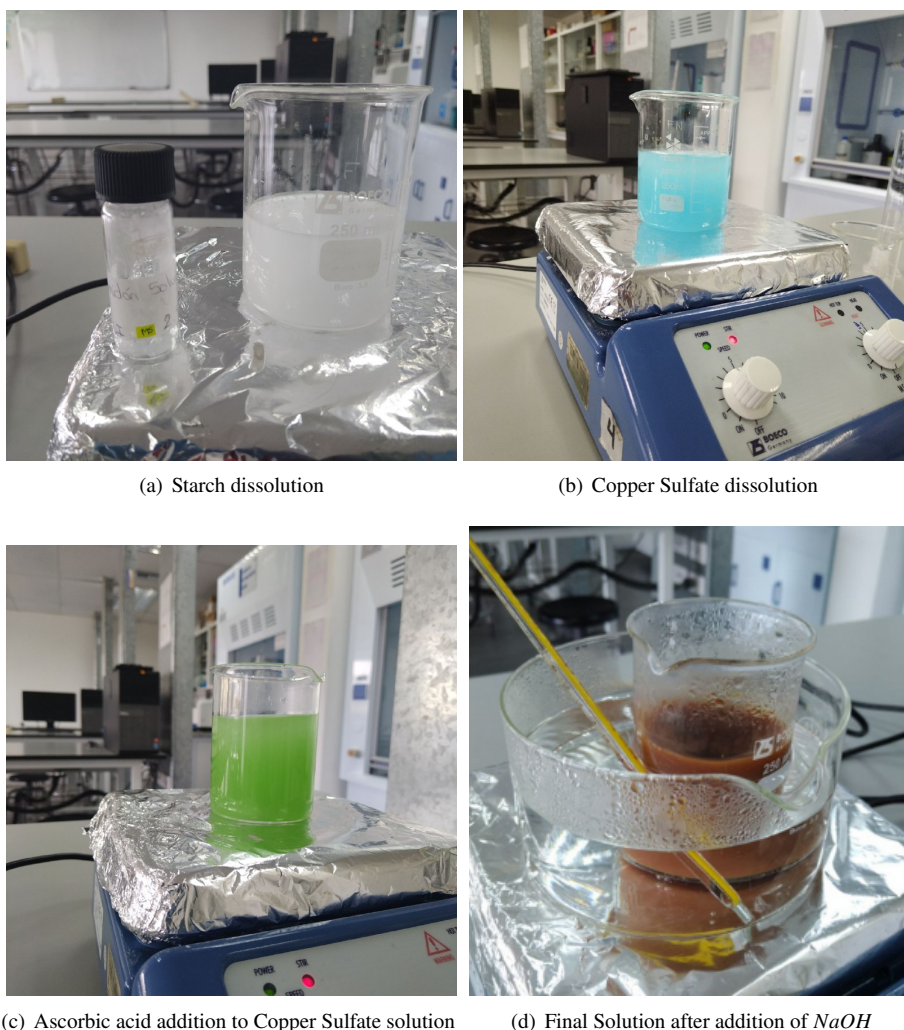
For synthesis of cupric oxide ( $Cu_2O$ ) and cuprous oxide ( $CuO$ ) NPs the work of Khan (2016)<sup>25</sup> was followed to obtain the next protocol. Copper oxides I and II NPs were obtained by chemical and physical process where  $CuSO_4 \cdot 5H_2O$  solution at 0.1 M, starch ( $C_6H_{10}O_5$ ) at 1,2%, ascorbic acid ( $C_6H_8O_6$ ) at 0.2 M and sodium hydroxide ( $NaOH$ ) at 1 M were the reagent employed. All the material was provided by Yachay Tech University and Nanotechnology laboratory. In 140 ml of distilled water was added 2.5 grams of starch that was vigorous stirring for 30 minutes before to added 3.5 g of copper (II) sulfate pentahydrated for other 30 minutes. The next step, 58 ml of 0.2 M ascorbic acid solution was incorporated in the solution in constant stirring and heating at 80 ° C for 2 hours, a color change form yellow to grayish brown is showed. In the heating process, the solution of sodium hydroxide was added slowly and pH measured employing pH paper.

Table 3.1: NaOH mL added vs pH

| Time (min) | NaOH (ml) | pH | Temperature (° C) |
|------------|-----------|----|-------------------|
| 0          | 0         | 1  | 70                |
| 5          | 5         | 1  | 75                |
| 9          | 10        | 2  | 78                |
| 13         | 15        | 3  | 80                |
| 18         | 20        | 4  | 78                |
| 22         | 25        | 5  | 78                |
| 27         | 30        | 7  | 78                |
| 30         | 35        | 10 | 79                |

After the 2 hours, the solutions stood for 30 minutes. The sample was spin-dry to 900 rpm for 10 min. In this step was separate copper oxide NPs to the solution before to be washed with distilled water and ethanol and putted in the spin-dry again until the NPs do not show any turbidity. The sample was prepared to be characterized by X-Ray Diffraction technique. The results have been discussed in the next chapter but they show a  $Cu^+$  NPs formation.

Thermal treatment is a technique that promotes change in molecular structure of metallic nanoparticles that permits obtain alloys. In the study case, the thermal treatment of copper nanoparticles is a crucial step in their transformation into copper oxide nanoparticles ( $Cu_2O$  and  $CuO$ ). Initially, the copper nanoparticles are synthesized using a chemical reduction method. Subsequently, they undergo a calcination process at different temperatures to induce the oxidation of copper and form copper oxides with distinct structural and optical properties.



(a) Starch dissolution

(b) Copper Sulfate dissolution

(c) Ascorbic acid addition to Copper Sulfate solution

(d) Final Solution after addition of NaOH

Figure 3.1: Chemical elaboration of copper NPs process.

First, the samples are calcined at  $350^{\circ}\text{C}$  for one hour. This thermal process facilitates the formation of cuprous oxide ( $\text{Cu}_2\text{O}$ ) from metallic copper nanoparticles. X-ray diffraction (XRD) peaks for these samples reveal the presence of  $\text{Cu}^+$ ,  $\text{Cu}_2\text{O}$ , and to a lesser extent,  $\text{CuO}$ , indicating that the initial oxidation primarily results in  $\text{Cu}_2\text{O}$  formation<sup>26</sup>.

To promote further oxidation and the formation of cupric oxide ( $\text{CuO}$ ), the samples are calcined at a higher temperature of  $600^{\circ}\text{C}$ , also for one hour. This more intense thermal treatment significantly reduces the  $\text{Cu}^+$  peaks while the peaks corresponding to  $\text{Cu}_2\text{O}$  and  $\text{CuO}$  become more prominent. Notably, there is substantial formation of  $\text{CuO}$ , suggesting that at elevated temperatures,  $\text{Cu}_2\text{O}$  undergoes further oxidation to form  $\text{CuO}$ <sup>27,28</sup>.

Using different calcination temperatures allows for the control of the  $\text{Cu}_2\text{O}$  and  $\text{CuO}$  ratio in the resulting nanoparticles, which is essential for tailoring their optical and electronic properties to meet specific requirements in optoelectronic device applications. For this reason the sample was divided in two samples and pass through a calcination process. The first sample was calcinated to  $350^{\circ}\text{C}$  for 1 hour until the next sample was calcinated to  $600^{\circ}\text{C}$  for 1 hour. Both samples were characterized by X-Ray Diffraction technique and UV-vis diffusive reflection technique.

Particle size was obtained by Scherrer equation:

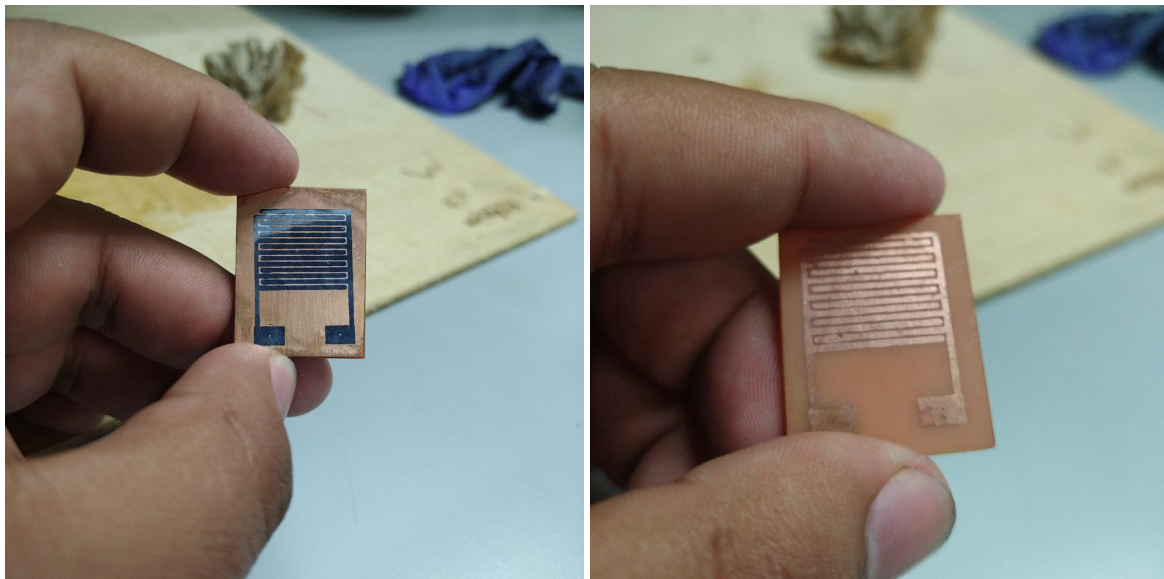
$$D = \frac{K \cdot \lambda}{\beta \cdot \cos(\theta)} \quad (3.1)$$

Where:

- **D (Crystal size):** This is the average size of the crystalline domains (in nanometers). It gives an estimation of the crystal size from the broadening of X-ray diffraction peaks. Smaller crystal sizes result in broader peaks.
- **K (Scherrer constant or shape factor):** This is a dimensionless constant that depends on the shape of the crystal.
- $\lambda$  (**X-ray wavelength**): This is the wavelength of the X-rays used in the diffraction experiment. For X-rays produced by copper (Cu  $K\alpha$ ),  $\lambda$  is approximately  $1.54 \text{ \AA}$ .
- $\beta$  (**Full width at half maximum, FWHM**): This represents the broadening of the diffraction peak at half its maximum intensity. The broadening is due to the finite size of the crystalline domains and must be corrected for instrumental broadening. It is measured in radians.
- $\theta$  (**Bragg angle**): This is the angle at which the X-ray beam is diffracted by the crystal planes, usually given in degrees but must be converted to radians for the Scherrer equation. It corresponds to the peak position in the diffraction pattern<sup>29</sup>.

### 3.1.2 Interdigitates Elaboration

For this research work was necessary the fabrication of copper based interdigitates following the next procedure. A PCB board was designed and printed in a couche paper. Second, a copper plate was prepared using a 600-grit water sandpaper to clean burr present in the edges of the plate before to transfer the PCB print using an iron for 5 minutes with slowly moves. Once the plate was ready, it was put in water for 20 minutes until the paper present a fragility before to carefully remove it to the plate. The ink was transferred to the copper plate, it is important try to clean the channels to guarantee the correct chemical remove of copper in the plate. After that plate was dry, it was employed ferric chloride solution where the plate was submerged until all the copper, except it over the ink, was removed. Finally, the copper cover by the ink was cleaned rigorously with thinner to obtain the interdigitate copper pattern.



(a) Pre-treatment Interdigitate

(b) Final Interdigitate result

Figure 3.2: Interdigitated fabrication process. The process includes the design, cleaning, pattern transfer, and chemical etching to obtain the interdigitated pattern on the copper plate.

### 3.1.3 Chitosan $Cu_2O/CuO/Cu+$ and $CuO/Cu_2O$ films fabrication

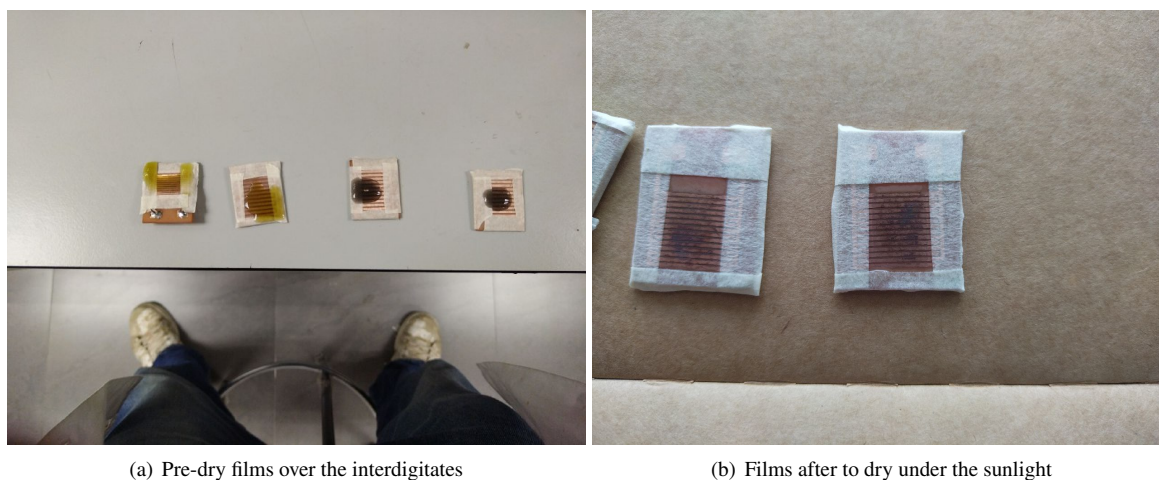
For the elaboration of a chitosan film, a solution of 1% of glacial acetic acid with a 1% of chitosan was prepared following the next protocol:

In a beaker of 250 ml added a 198 ml of distilled water with 2 ml of glacial acetic acid. This beaker was stirring for 5 minutes before to add 2 g of half-molecular mass chitosan. When chitosan was added then was rigorously stirring for 2 hours until the solution do not present lumps floating. The chitosan solution was left at rest for a night to avoid the presence of bubbles of air in the liquid. Next, a different metal NPs proportions films were elaborated to determine which concentration and blend present the best photoconductance showed in Fig.3.2:

Table 3.2: Metal NPs percentage on interdigitates in function of their mass/volume

| $Cu_2O$ (g/ml) | $CuO$ (g/ml) |
|----------------|--------------|
| 1.005%         | 1.065%       |
| 2.72%          | 2.63%        |
| 5.45%          | 5.26%        |

These concentrations were treatment with ultrasound for 30 minutes to promote the dispersion of NPs in the chitosan solution. Meanwhile, interdigitates were cover with tape to delimited the dispersion of the film onto the electrodes. The solution was put over the circuits to by distribute uniformly employing a microscope slide and leave over the sunlight until they dry as it is showed in Fig.3.3. Once the interdigitates are complete dry were measure their photoconductance employing a homemade DAQ "NI USB-6210" Circuit.



(a) Pre-dry films over the interdigitates

(b) Films after to dry under the sunlight

Figure 3.3: Fabrication process of chitosan films with copper oxide nanoparticles. The process involves the preparation of a chitosan solution, incorporation of nanoparticles, and application on the interdigitated electrodes, followed by drying under sunlight.

### 3.1.4 Equipment used to characterized

The research employed sophisticated equipment to synthesize, characterize, and analyze the  $Cu_2O-CuO$ -chitosan composite films. The Rigaku MiniFlex 600 X-ray Diffractometer showed in Fig.3.4 was used to determine the crystal structure of nanoparticles. This equipment operates with a 600W X-ray tube and a Bragg-Brentano goniometer with an 8-position auto-sampler, utilizing a  $CuK\alpha$  sealed tube as the radiation source. The measurement conditions were set at 40 kV and 15 mA, with a scanning range of  $20^\circ$  to  $100^\circ$  in  $2\Theta$  and a step size of  $0.01^\circ$ .





Figure 3.4: Rigaku MiniFlex 600 X-ray Diffractometer taking the measure of the first synthesis sample

Optical properties were analyzed using a PerkinElmer LAMBDA 1050 UV/Vis/NIR Spectrophotometer. This spectrophotometer was employed to measure the optical transmittance of the samples at a scanning speed of 50 nm/s across the 200–1100 nm wavelength range. The reflectance was analyzed in the UV (200 nm) to visible (1100 nm) regions.

Centrifugation was performed with a Sorvall Legend XTR Centrifuge from Thermo Scientific. Calcination was made employing mufla model MRC. A homemade circuit followed by the DAQ "NI USB-6210" was used for photoconductance measurements.

A second batch of metallic copper NPs was fabricated follow the previously methodology with the objective to obtain more material for the films. The compare with the first batch was analyzed in the next chapter.

### 3.2 DAQ "NI USB-6210" Circuit

To measure the photoconductance of the interdigitates, the circuit shown in Fig. 3.5 has been designed to detect low current signals. The interdigitates are powered by a stable and noise-free 9V battery (B1) and are connected to a voltage divider network formed by resistors R1 to R6, which regulates the input signal level. The conditioned signal is sent to an operational amplifier (U2), configured as a voltage follower to buffer the input and maintain high input impedance. After buffering, the signal passes through a diode protection network (D1 and D2) to protect the subsequent stages from possible voltage spikes.

The signal is then routed through a second operational amplifier (U2) configured as a non-inverting amplifier with feedback from resistors R7 and R11, which amplifies the signal. The amplified signal is further processed in a third amplification stage using operational amplifier U5. The gain of this stage is adjusted via the RV1 potentiometer, allowing the signal to match the dynamic range required by the data acquisition (DAQ) system. The final output is routed to the DAQ system for digitization and analysis. The circuit design ensures that the measurements are reliable by maintaining signal integrity across all stages. A manual system was used with the aim of interrupting the passage of light from a white LED light source at constant time intervals to determine the direct influence of light on the films. Finally, three light filters (red, blue, and green) were used after the control sample to determine the influence of specific ranges of the visible spectrum. This will be discussed in the results chapter.

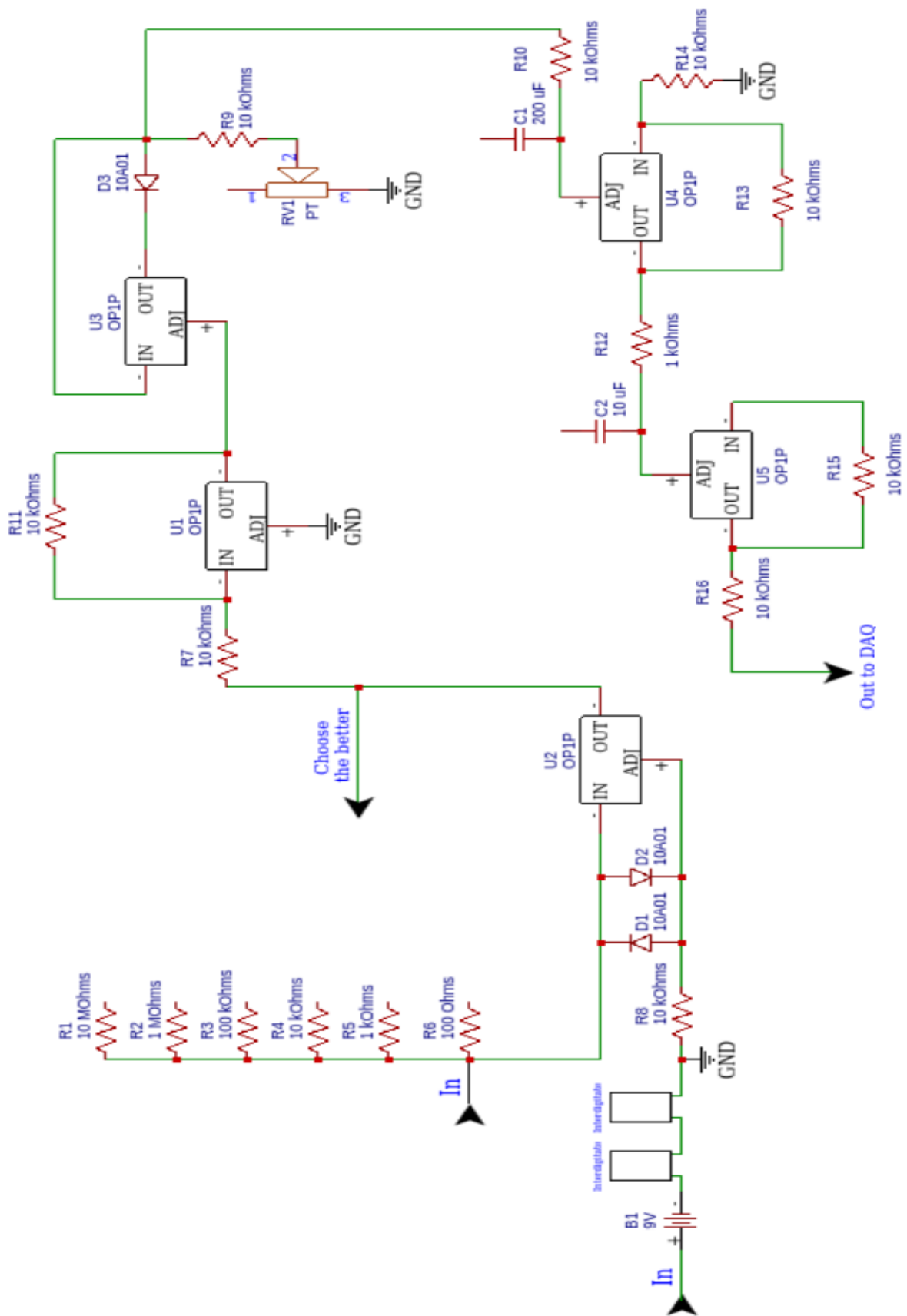


Figure 3.5: DAQ Circuit Diagram

# Chapter 4

## Results

All the data-sheets recollected during the research were analyzed and plotted employing Google Colab software and numpy, panda, sciphy, matplotlib libraries.

### 4.1 XRD

In Figure 4.1, the X-ray diffraction (XRD) pattern of the first sample synthesized using the described methodology is presented. The diffractogram reveals principal peaks corresponding to various copper oxide phases, specifically  $Cu^+$ ,  $Cu_2O$ , and  $CuO$ , identified in accordance with the International Center for Diffraction Data (ICDD) standards.

The peaks at  $43.3^\circ$ ,  $50.4^\circ$ , and  $74.1^\circ$  are characteristic of  $Cu^+$  nanoparticles (NPs), correlating with the (111), (200), and (220) crystal planes, respectively identify as the red triangle icon. Additionally, four distinct peaks at  $36.5^\circ$ ,  $42.2^\circ$ ,  $61.4^\circ$ , and  $74.2^\circ$  are identified, typical for  $Cu_2O$  NPs recognized as blue triangle icon. These peaks correspond to the (111), (200), (220), and (311) crystallographic planes, suggesting the formation of well-defined crystalline structures.

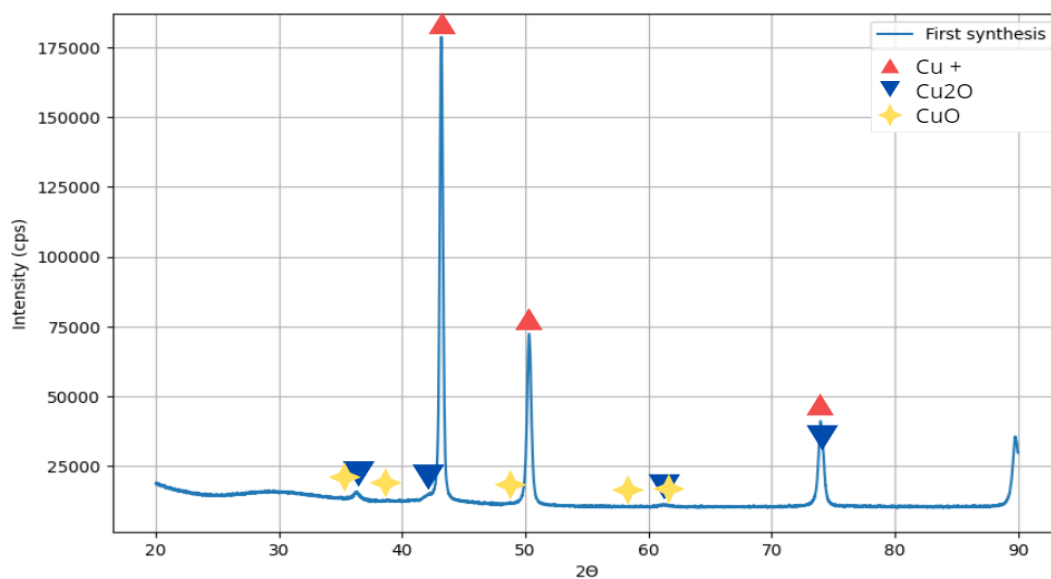


Figure 4.1: X-ray diffraction (XRD) pattern of the first synthesized sample, showing the characteristic peaks corresponding to  $Cu^+$ ,  $Cu_2O$ , and  $CuO$  phases. The analysis provides insight into the structural composition and phase purity of the nanoparticles.

Interestingly, while the  $Cu^+$  and  $Cu_2O$  phases are clearly represented in the sample, no discernible peaks for  $CuO$  were detected in the spectrum. This absence indicates a selective synthesis that predominantly favors the formation of  $Cu^+$  and  $Cu_2O$  under the experimental conditions employed. The precise identification of these phases is crucial for understanding the physicochemical properties of the synthesized material and its potential applications in various technological fields. The zones where  $CuO$  peaks are to be present are identified with a yellow star icon in Fig.4.1

In Figure 4.2, the X-ray diffraction (XRD) pattern of the sample calcinated at 350 °C is presented. This analysis provides a comprehensive view of the crystallographic changes induced by moderate thermal treatment. The diffractogram exhibits characteristic peaks for three different types of copper-based nanoparticles:  $Cu^+$ ,  $Cu_2O$ , and  $CuO$ .

For the  $Cu^+$  phase, there is a noticeable reduction in peak intensity, suggesting a partial transformation or reduction of this phase under the applied temperature conditions. In contrast, the peaks corresponding to  $Cu_2O$  show an increase in intensity, indicating enhanced crystallization or stabilization of this phase at 350 °C.

Most notably, the emergence of new peaks at 35.5°, 38.7°, 48.9°, 58.3°, and 61.6°, predominantly attributes to the  $CuO$  phase, significantly marking the formation of this oxide. These peaks correspond to the (002), (111), (202), (020), and (113) crystal planes, respectively, showcasing the diversity and complexity of the crystal structures forming within this sample.

The presence of these peaks denote a phase evolution influenced by the different employed temperatures in calcination process, highlighting the transformation from  $Cu^+$  and  $Cu_2O$  to the more stable  $CuO$  phase. This transformation is desirable for the applications where the electrical and catalytic properties of  $CuO$  are needed. The analysis underscores the balance of thermal treatment in achieving desired material phases.

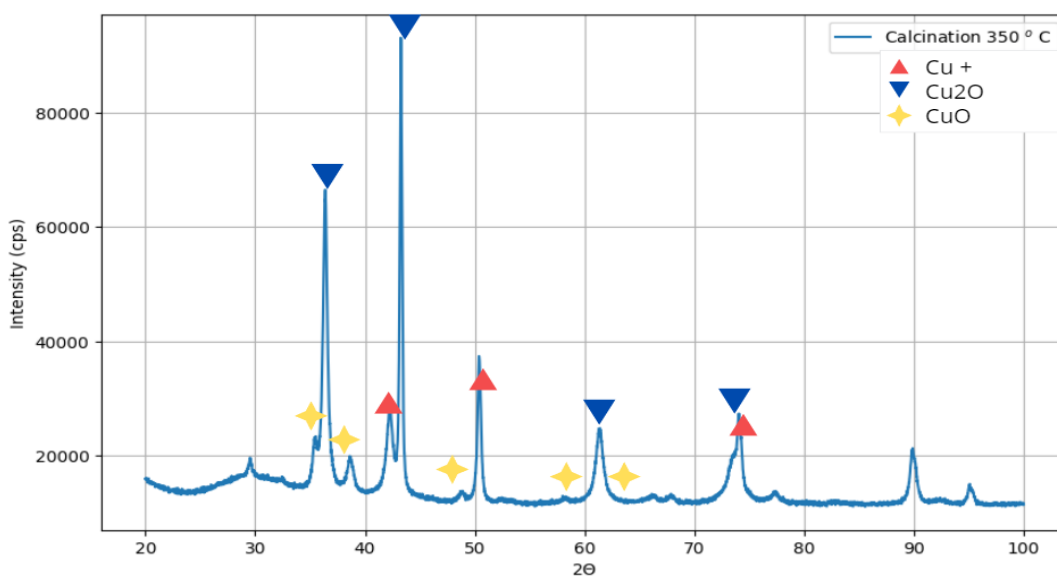


Figure 4.2: X-ray diffraction (XRD) analysis of the sample calcinated at 350°C for one hour. This figure reveals the emergence of  $Cu_2O$  and  $CuO$  phases, with reduced intensity of  $Cu^+$  peaks, demonstrating the effect of thermal treatment on the nanoparticle structure.

In Figure 4.3, the X-ray diffraction (XRD) analysis of the sample subjected to calcination at 600 °C is depicted. This thermal treatment significantly influences the crystalline phases present within the sample. Notably, the intensity of the  $Cu^+$  peaks has dramatically reduced, nearing the threshold of detectability, which suggests a decomposition or transformation of the  $Cu^+$  phase under the applied thermal conditions.

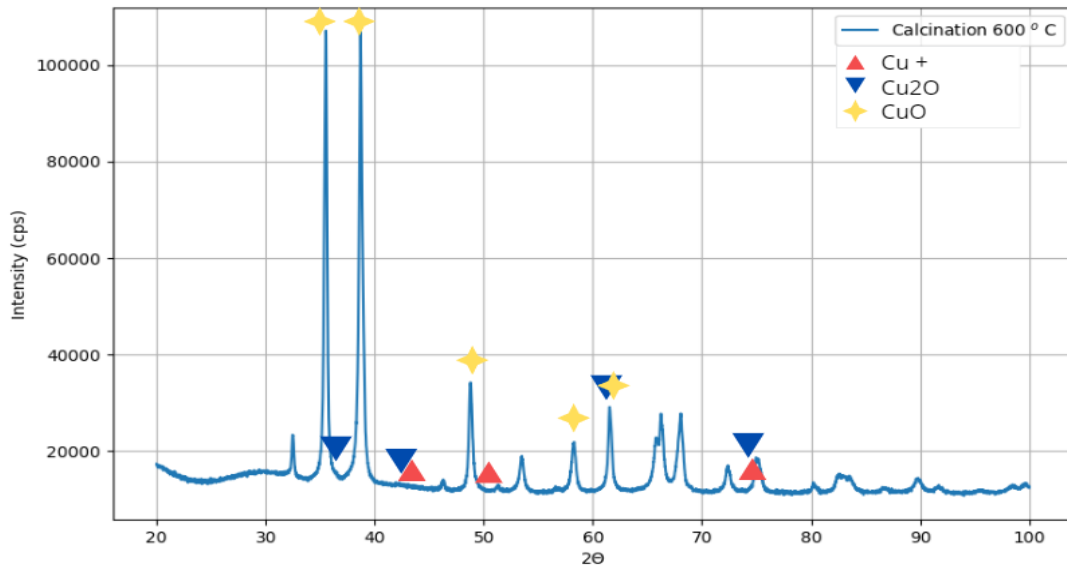


Figure 4.3: XRD 600 ° C for 1 hour sample

Simultaneously, the peaks associated with  $Cu_2O$  exhibit a lower intensity compared to the pristine sample, indicating a partial reduction or transformation of  $Cu_2O$  at this elevated temperature. In stark contrast, the peaks corresponding to  $CuO$  show a significant increase in intensity across the diffractogram. Peaks at  $35.5^\circ$ ,  $38.7^\circ$ ,  $48.9^\circ$ , and  $58.3^\circ$ , corresponding to the (002), (111), (202), and (113) planes of  $CuO$ , respectively, are markedly pronounced. This enhancement in peak intensities clearly denotes the formation or growth of the  $CuO$  phase, which becomes the dominant crystalline structure in the sample post-calcination.

The shifting of peak intensities and the emergence of new peaks at 600 °C indicate a dynamic transformation within the sample, likely driven by the thermally induced oxidation processes. These transformations are crucial for applications requiring specific copper oxide phases, as the thermal treatment tailors the material's properties towards enhanced stability and performance in various applications such as catalysis, electronics, and energy storage.

In Figure 4.4, a comparative analysis of the X-ray diffraction (XRD) patterns for samples calcinated at 350 °C and 600 °C is presented. This comparison clearly illustrates the evolution of the copper-based phases under different thermal treatment conditions, offering insights into the material's behavior at varying temperatures.

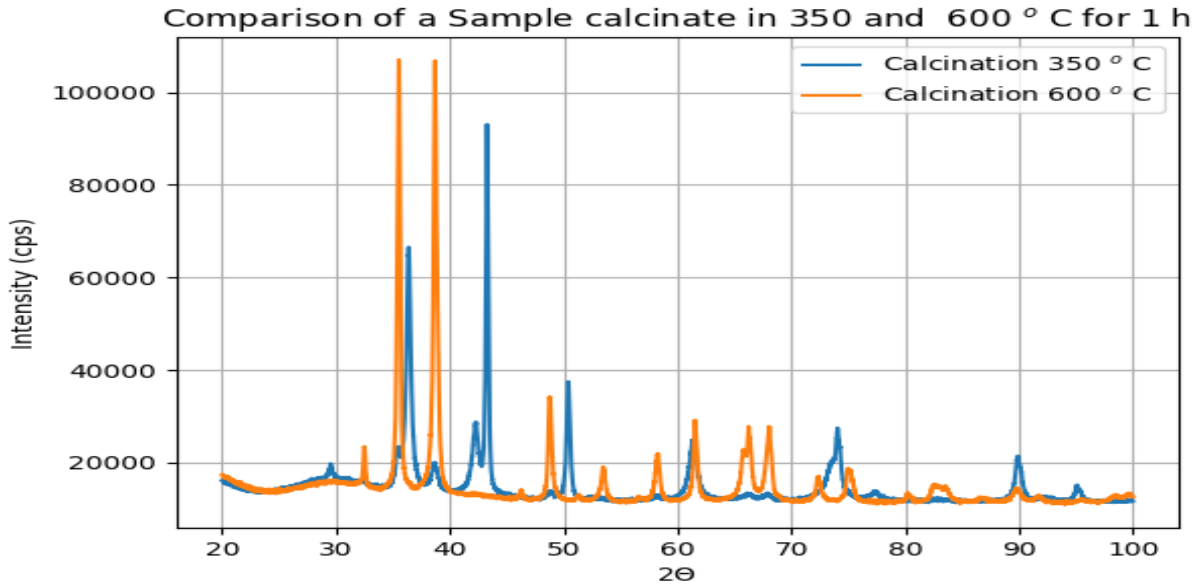


Figure 4.4: XRD comparison of 350 and 600 ° C calcinated samples

For the sample calcinated at 350 °C, the peaks associated with both  $Cu^+$  and  $Cu_2O$  are discernible, albeit with reduced intensity compared to the more robust peaks observed in the sample treated at 600 °C. This suggests a partial degradation or transformation of these phases at the lower calcination temperature, with incomplete crystallization or stability.

In contrast, the 600 °C sample exhibits a significant enhancement in the intensity and sharpness of the  $CuO$  peaks. The peaks corresponding to  $CuO$  not only become more pronounced but also demonstrate better crystallinity, as evidenced by their heightened and narrower peak profiles. The increased crystallinity at 600 °C indicates a more complete transformation and stabilization of the  $CuO$  phase, facilitated by the higher temperature which likely drives the oxidation and rearrangement of the crystal lattice more effectively.

This comparative diffractogram underscores the critical impact of temperature on the phase composition and crystallographic properties of copper oxides. The transformation from  $Cu^+$  and  $Cu_2O$  to the more thermally stable  $CuO$  is markedly favored at 600 °C, reflecting the utility of thermal treatment in tailoring material properties for specific applications, such as in catalysis or electronic materials where the purity and crystallinity of phases play a vital role.

The average particle size of each sample synthesized and subsequently calcinated at different temperatures was meticulously calculated using Python programming language. In Google Colab environment scipy package was employed to find the peaks with an intensity over 16 000 cps. Then, using Scherrer Equation in Eq.3.1 with  $K = 0.9$  (Scherrer constant) and  $\lambda = 1.54\text{\AA}$  (X-ray wavelength for Cu  $K\alpha$  radiation), the results were saved in a DataFrame with pandas package to finally calculated the average size of each sample. These computations provide quantitative insights into the effects of thermal treatment on the particle dynamics within copper oxide systems. The summarized results are as follows:

Table 4.1: Average particle size of each sample

| Sample          | Average Particle Size (nm) |
|-----------------|----------------------------|
| First Synthesis | 55.75                      |
| $Cu_2O$         | 63.32                      |
| $CuO$           | 68.18                      |

The initial synthesis yielded nanoparticles with an average diameter of 55.75 nm. Following this, samples subjected to calcination at 350 °C exhibited a slight increase in particle size to 63.32 nm. This increase can be attributed to the

sintering effect where particles may coalesce or grow due to the thermal energy provided, despite being at a relatively moderate temperature. The growth in particle size is consistent with the observed intensification of  $Cu_2O$  peaks in the XRD patterns, suggesting enhanced crystallization at this temperature.

Further calcination at 600 °C led to a more pronounced increase in particle size, reaching an average of 68.18 nm. This significant growth is indicative of a higher degree of sintering and crystalline transformation, supported by the sharp and intense peaks of  $CuO$  observed in the XRD analysis. At this elevated temperature, the particles not only increase in size but also likely undergo a phase transformation, leading to a more stable  $CuO$  phase which is evident from the enhanced crystallinity and particle cohesion.

These findings underscore the critical influence of calcination temperature on the morphological and structural characteristics of copper oxide nanoparticles. Such changes are crucial for tailoring the properties of the material for specific applications, where particle size and phase purity can significantly impact catalytic activity, electronic properties, and material stability. The precise control of particle size through thermal treatment provides a valuable tool for optimizing material performance in various technological domains.

## 4.2 UV-Vis Spectroscopy

Both samples were analyzed using diffuse reflectance method due to the samples are in powder state. The employed machine give us the result of Kubelka-Munk transformation to transform reflectance into absorption to be analyzed in Fig.4.5 where it is possible to appreciate a notable difference between them. 600 °C calcinated sample show a better absorption in compare with 350 °C calcinated sample.

The sample calcinated at 350 °C shows distinct absorption peaks, particularly prominent in the lower wavelength range. This feature could be attributed to the electronic transitions within the  $Cu_2O$  phase, which is known for its bandgap around 2.0 eV to 2.2 eV (corresponding to wavelengths of about 560 nm to 620 nm). The presence of sharp peaks in this region may indicate a relatively high degree of crystallinity and purity of the  $Cu_2O$  phase at this calcination temperature.

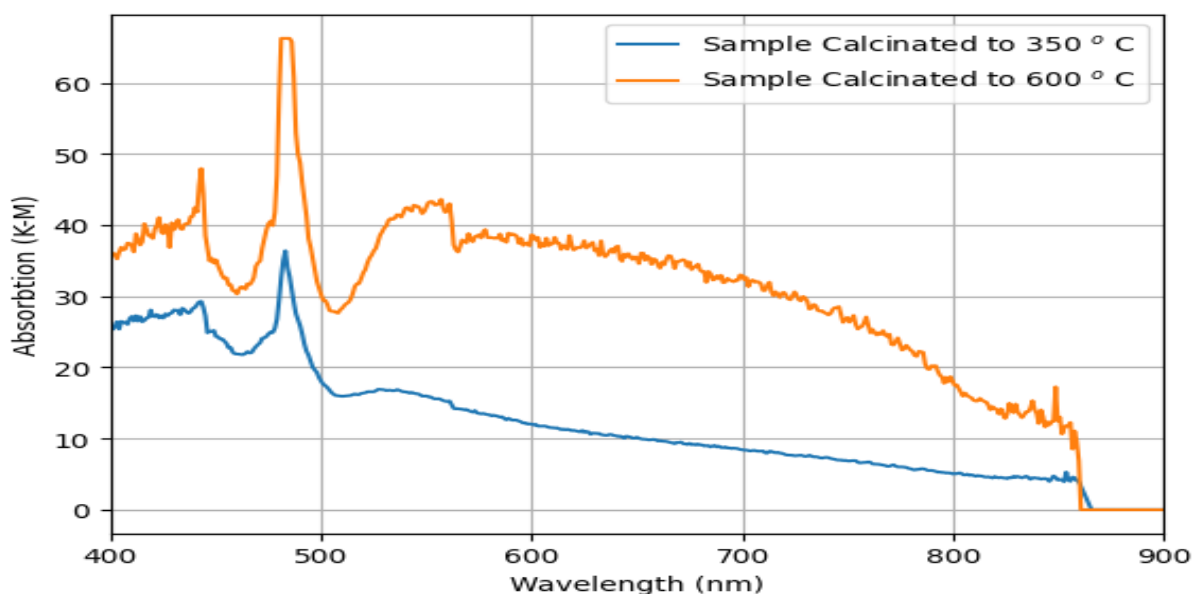


Figure 4.5: Absorption vs Wavelength UV-Vis spectrum comparison between samples

The sample calcinated at 600 °C, in contrast, exhibits a smoother spectrum with a broad absorption band that extends over a larger wavelength range. The tailing towards longer wavelengths and the overall higher absorption intensity

across the spectrum could be indicative of the formation of  $CuO$ , which has a narrower bandgap (about 1.2 eV to 1.7 eV, corresponding to wavelengths of approximately 730 nm to 1030 nm). The broader and smoother absorption profile suggests a more continuous distribution of electronic states, typical of more complex or disordered structures.

The increase in particle size with higher calcination temperature, as previously noted in Fig.4.1, could also be influencing the optical properties observed in the spectra. Larger particle sizes in the sample calcinated at 600 °C might be contributing to the broader absorption characteristics due to less pronounced quantum confinement effects compared to the smaller particles in the 350 °C sample.

Additionally, the difference in peak shapes and intensities between the two samples can be associated with the different phases and their distributions. More crystalline phases often display sharper spectral features, whereas more amorphous or mixed-phase materials exhibit broader, less defined absorption features.

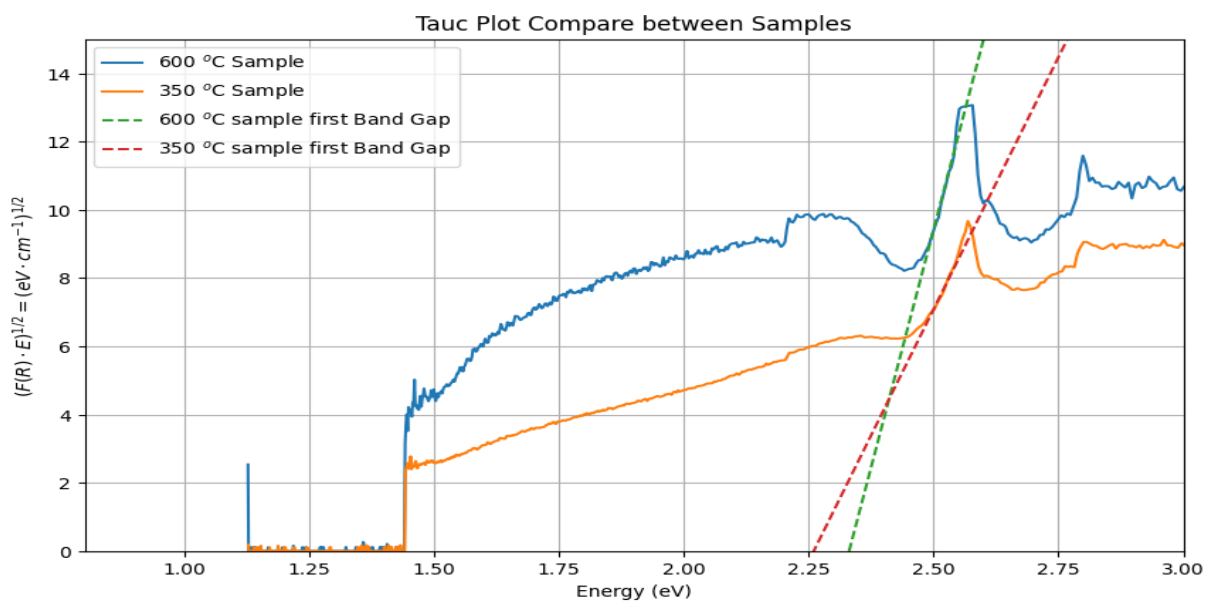


Figure 4.6: Tauc Plot Comparison between samples recognized the first bandgap of each sample.



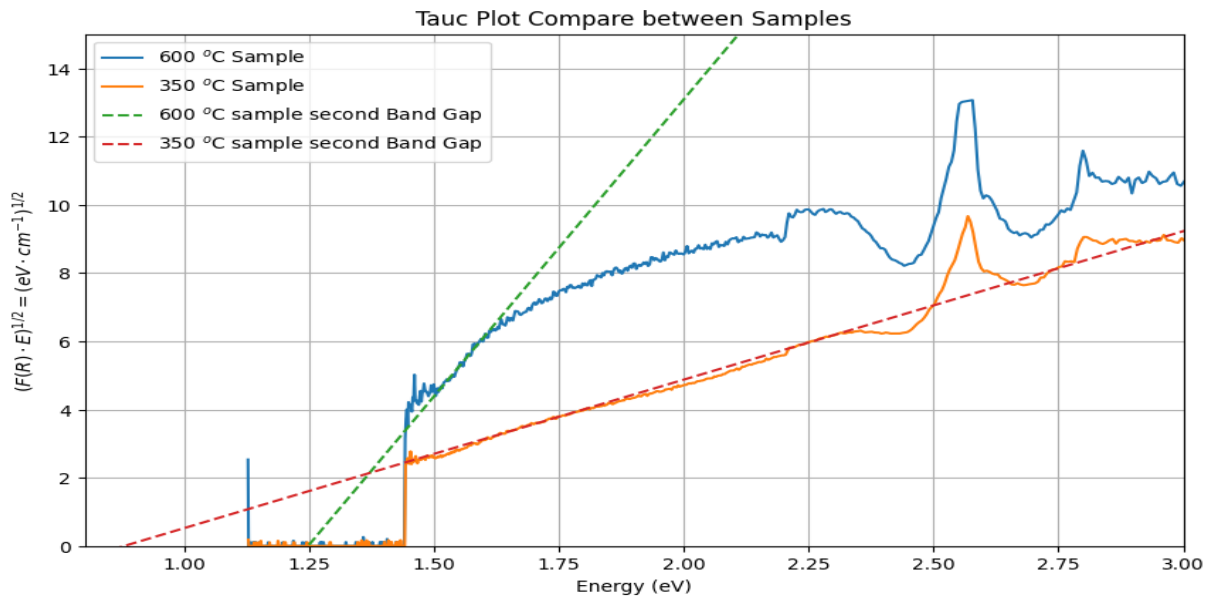


Figure 4.7: Tauc Plot Comparison between samples recognized the second bandgap of each sample.

Fig.4.6 shows a Tauc Plot based in the information obtained in Fig.4.5 where in 350 °C sample, the Tauc plot shows a gradual increase in the  $[F(R) \cdot E]^{1/2}$  function starting at lower energy levels, suggesting a wider bandgap compared to the 600 °C sample. This wider bandgap indicates a potential for applications requiring UV light absorption.

Conversely, the 600 °C sample exhibits a steeper rise in the  $[F(R) \cdot E]^{1/2}$  function, beginning at higher energy levels, which implies a narrower bandgap. This characteristic is beneficial for applications that operate within the visible to near-infrared spectrum, enhancing the material's suitability for photocatalytic and electronic applications.

The plots also reveal specific electronic transitions and defects within the crystal structure of the materials, indicated by peaks and troughs in both samples around 2.5 eV and higher. These features suggest changes in the crystallinity and phase purity due to the calcination process.

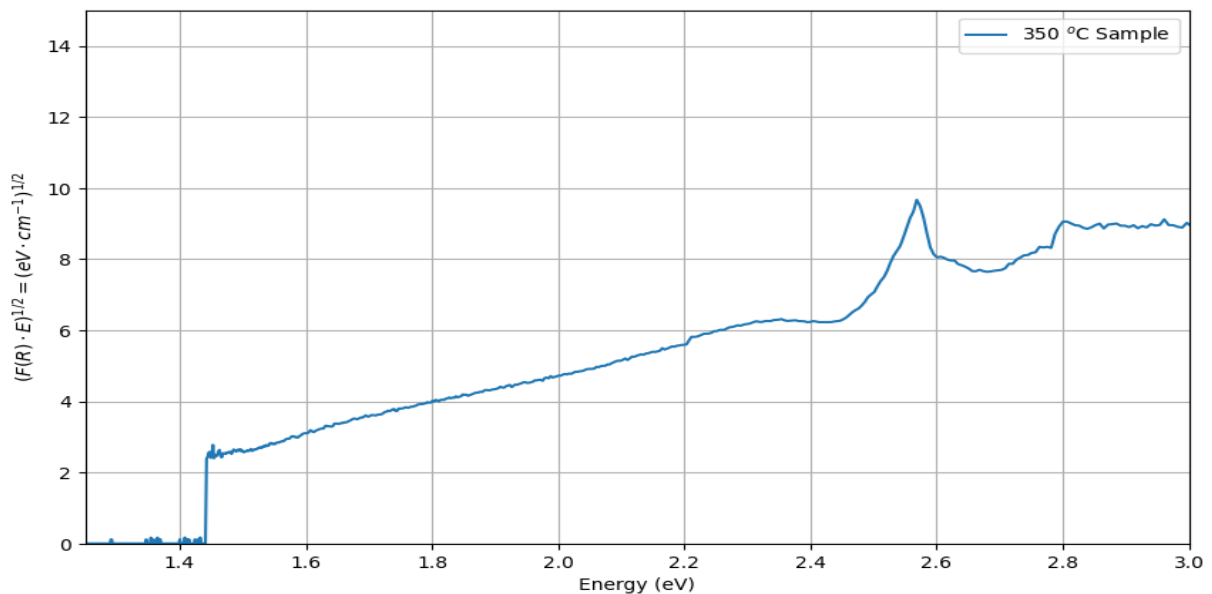


Figure 4.8: Tauc Plot of 350 °C calcinated sample

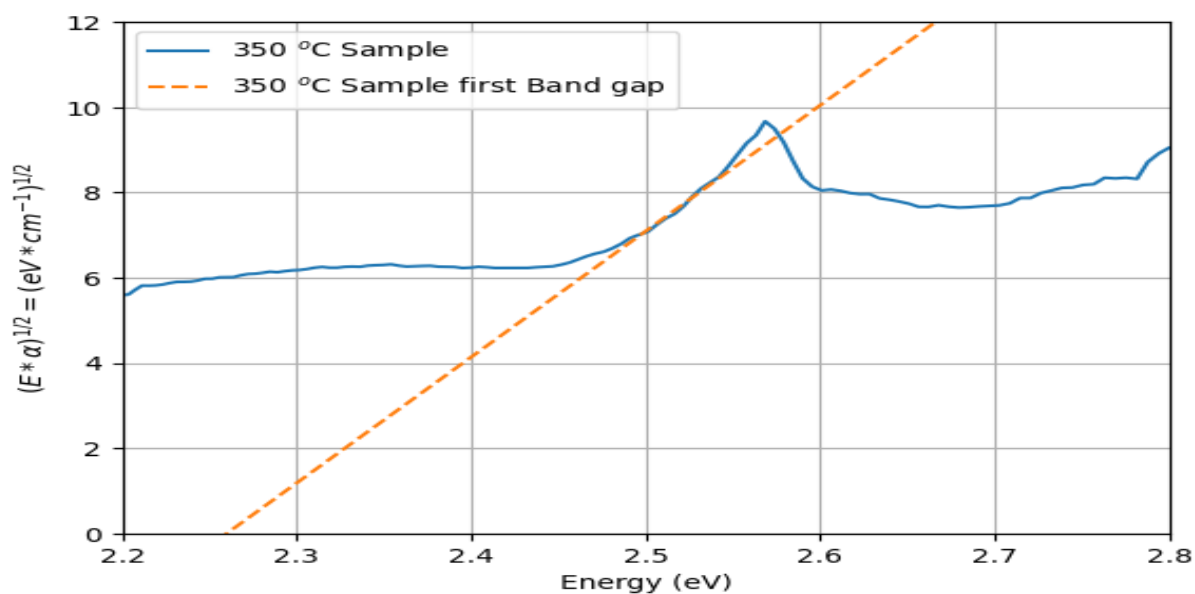


Figure 4.9: First Band Gap recognized in Tauc Plot of 350 °C

In Fig.4.8 was appreciate a shoulder increase in 2.4 to 2.5 eV that matches with the results presented in (Zayed. M. F. 2020) research. In this investigation employs a different synthesis method resulting in a sample of  $Cu_2O$  metallic NPs with less impurities than the sample obtained in the laboratory. The result reported in Absorbance in the work of Zayed has a big similitude with the results obtained in the present research showed in Fig.4.5, specially to 350 °C calcinated sample. Also, the Tauc Plot in Zayed work present a band gap in a Value of 1.9 eV that are close to the first band gap of both samples<sup>30</sup>.

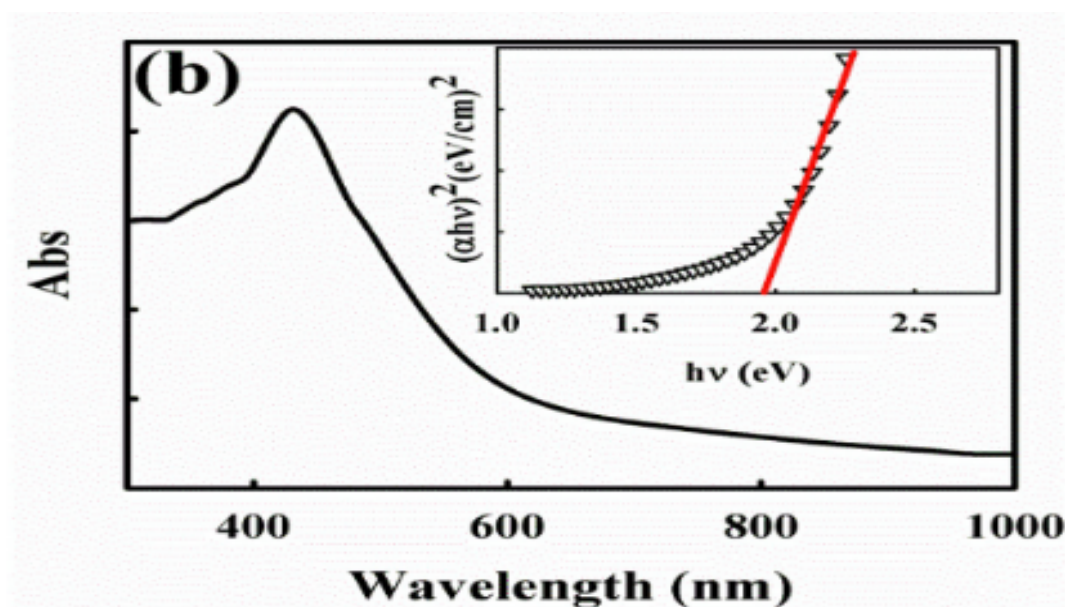


Figure 4.10: UV-vis spectrum with the inset is the Tauc plot pattern of a  $Cu_2O$  NPs sample recover from (Zayed. M. F. 2020)<sup>30</sup>

The calcination temperature of 350 °C was sufficient to achieve crystallization of  $Cu_2O$  without transitioning predom-

inantly to  $CuO$ , which has a narrower band gap. This temperature-specific phase stability is crucial for controlling the electronic properties of the material. The estimated band gap calculated was 2.260 eV see in Fig.4.9 that aligns well with the visible light spectrum, making this material an excellent candidate for light-harvesting applications. It can absorb a significant portion of the solar spectrum, which is desirable for solar energy converters and photocatalytic processes.

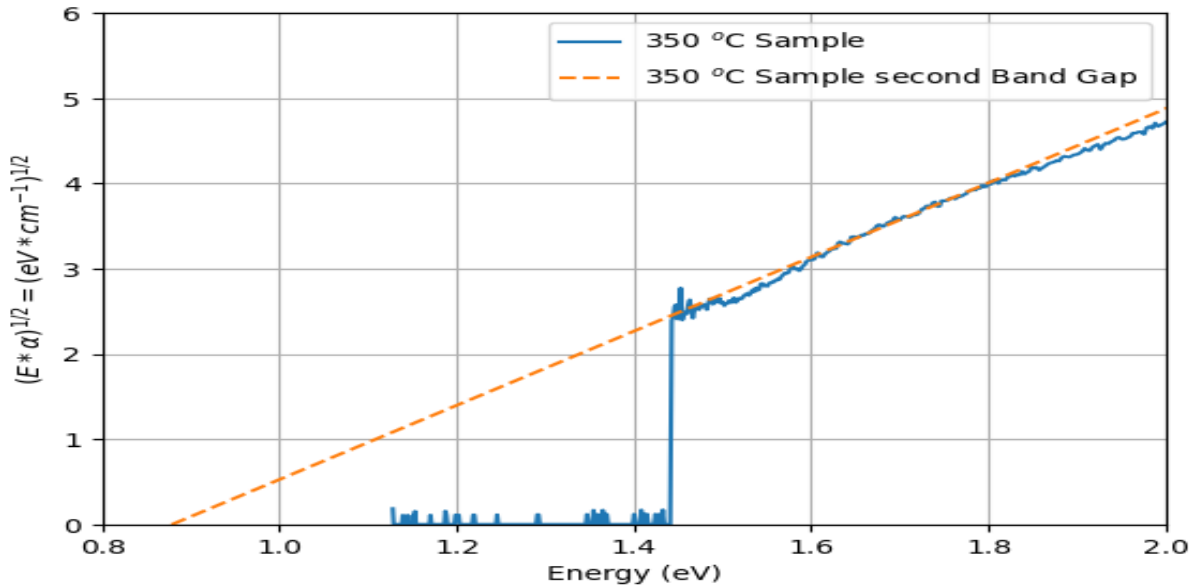


Figure 4.11: Second Band Gap recognized in Tauc Plot of 350 °C

On the second recognized band gap in 0.879 eV could be attributed to the presence of  $CuO$  NPs in the sample analyzed in Fig.4.2 due to this band gap is in Infrared spectrum own of this oxide. But it is not significantly in the photoelectric features of the sample due to the low amount of  $CuO$  present in the sample.

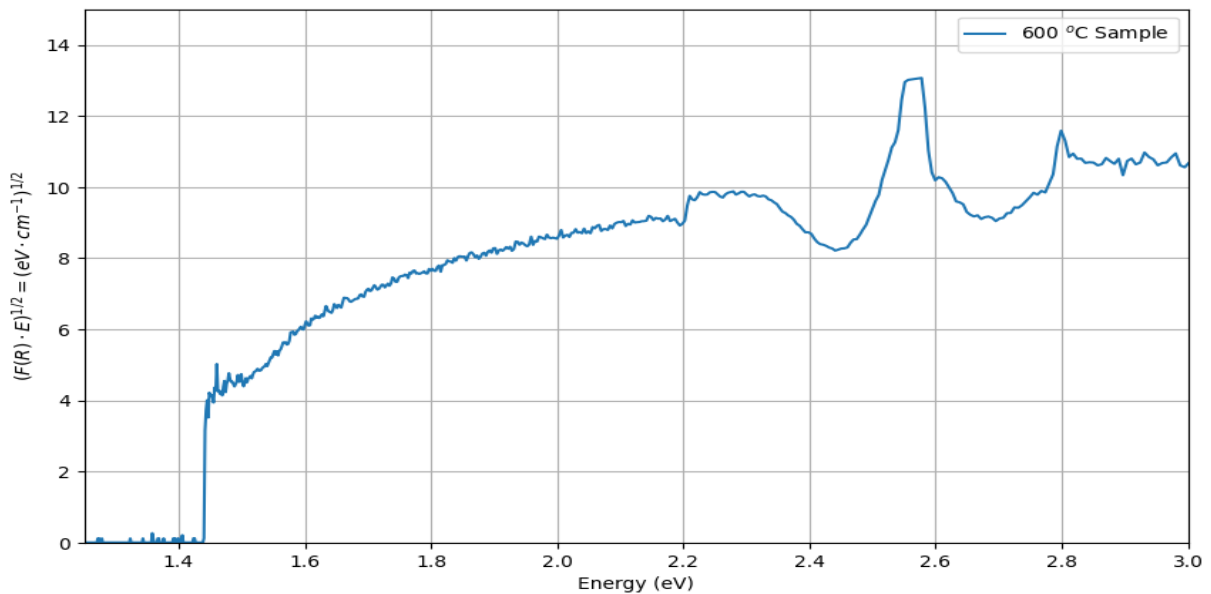


Figure 4.12: Tauc Plot of 600 °C sample

The Tauc Plot see in Fig.4.12 suggest that the material could be highly effective in photocatalytic applications, such

as degradation of pollutants under sunlight. The ability to absorb visible light enhances its activity under real-world conditions. Similarly, in electronic applications, a narrower bandgap can facilitate better charge carrier generation under normal lighting conditions, which is advantageous for photovoltaic cells and sensors. The graph shows a sharper increase in the function  $[F(R) \cdot E]^{1/2}$ , particularly noticeable as the energy level exceeds about 1.5 eV. This steeper rise suggests a more pronounced absorption onset.

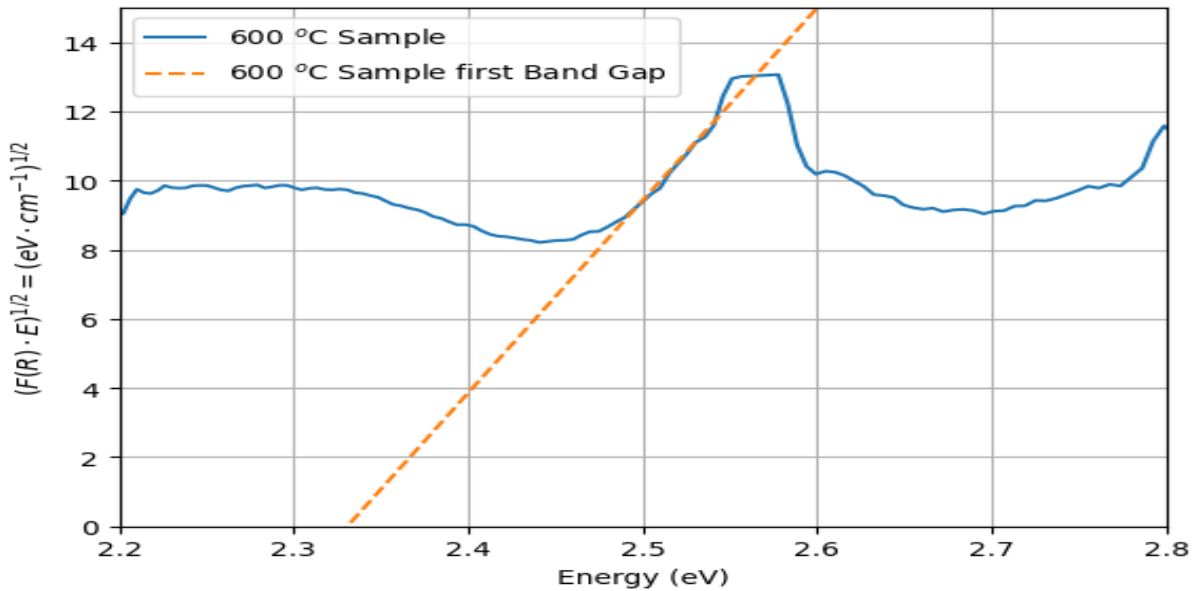


Figure 4.13: First Band Gap recognized in Tauc Plot of 600 °C

The first recognized band gap was 2.331 eV, that was similar to the results saw in Fig.4.9 where again aligns with the visible light spectrum, making this material an excellent candidate for light-harvesting applications. In compare with the last sample, 600 °C calcinated sample show a bigger absorption peak and a vertical tendency more remarkable in compare. Other consideration it is the fact that this sample show a valley between the peak and the rest of the curve in contrast with the flat curve between the absorption peak and the rest of the plot in 350 °C calcinated sample.

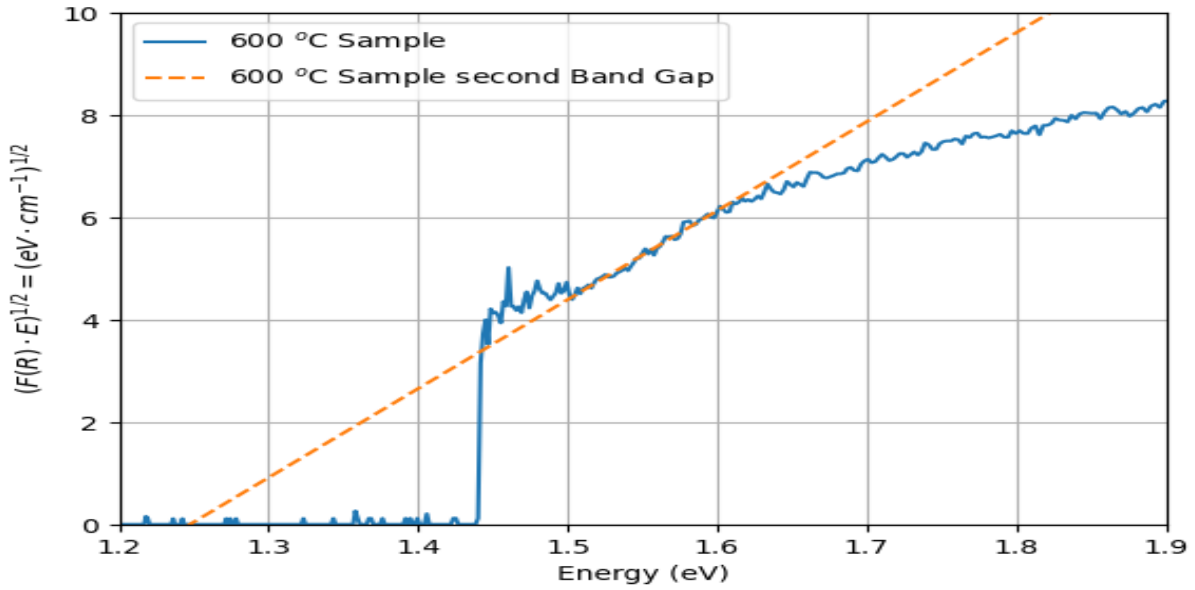


Figure 4.14: Second Band Gap recognized in Tauc Plot of 600 °C

Second band gap recognized was 1.248 eV, that makes sense when remember that this sample present *CuO* NPs as its principal component where the band gap is located in Infrared spectrum that helps to absorb a low energy photons present in the sunlight. This feature could be an advantage in contrast with the other sample. This point were analyzed in the next section.

The experimental findings for both samples are consistent with the experimental results reported by Heinemann (2013)<sup>31</sup>, who observed a band gap for *Cu<sub>2</sub>O* at 2.17 eV. These results align closely with the experimental values obtained at temperatures of 600 °C (2.331 eV) and 350 °C (2.5 eV). Similarly, for *CuO*, Heinemann (2013) documented a band gap of 1.4 eV, which compares to our experimental observations at 350 °C (0.879 eV) and 600 °C (1.248 eV). The variation in band gap values with temperature can be attributed to changes in electronic structure and lattice dynamics, influenced by thermal expansion and increased phonon activity. These results underscore the importance of temperature as a key factor in semiconductor properties, which can have significant implications for device performance and material applications.

### 4.3 Chitosan Films elaboration

In this process it is necessary to denote three points to take in consideration for future replications. The films show a big sensibility to the light source and in this first try 4 of the interdigitates present signals of corrosion after to be put under a cloudy sky see in Fig.4.15. The corrosion observed in the interdigitated structures seems to be related both to the lack of light exposure and the nature of the solution. Samples that were not sufficiently exposed to sunlight showed signs of corrosion, indicating that light is crucial for the proper drying of the chitosan films. Regarding the solution, while it contains 1% acetic acid, the pH is between 6 to 7 due to the low concentration of acid (that was confirmed by pH paper in the final solution). Therefore, the corrosion may not have been significantly influenced by the acidity of the solution, but rather by inadequate drying under light. The second point was the change of phase appreciated in 350 °C.

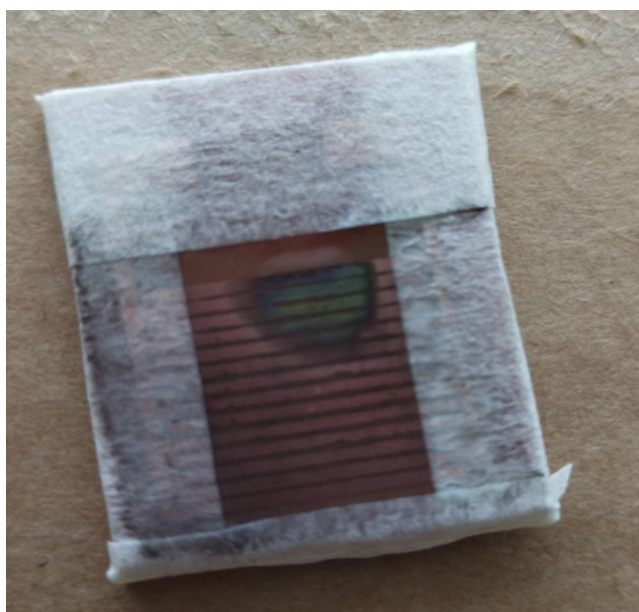


Figure 4.15: Corrosion produced by lack of sunlight



(a) 350 °C calcinated sample diluted in chitosan before to ultrasound treatment. (b) 350 °C calcinated sample diluted in chitosan after to ultrasound treatment.

Figure 4.16: Color comparison of the [chitosan/350°C] sample before and after ultrasound treatment. The left image shows the sample's dark coloration before treatment, while the right image shows the brick-like matte color after ultrasound treatment, indicating possible nanoparticle agglomeration.

Fig.4.16(a) shows how [chitosan/350°C] sample sample in a beginning present a dark coloration very similar to [chitosan/600°C] sample see in Fig.4.17 until that was treat in ultrasound equipment. After 30 minutes, the sample present a matte color similar to an old brick. This color is typically for copper oxide I, a hypothesis was put forward to explain this phenomena. In synthesis process was employed starch as a protector for copper NPs, it was possible that this factor produce an agglomeration between NPs that were cover by starch producing that in calcination process the black color was burned starch that cannot be removed while the washing process. Finally, ultrasound could break this agglomeration producing the color change. This idea is supported by NX7 Atomic Force Microscope of Yachay Tech University equipment measure

that was realized before the calcination process but requires a more detailed analyze that was not the objective of this research project but that was present in Appendix.



Figure 4.17: Comparative between 600 and 350 ° C calcinated samples after ultrasound treatment.

In Fig.4.17, [chitosan/600 °C] (left) and [chitosan/350 °C] (right) samples were put in back-lighting to denotes their difference in the colors minutes after to be treat in ultrasound. [chitosan/350 °C] sample has a particular feature because if we compare how its sample looks in Fig.4.16(b) it is possible to note a difference between its clarity. While in the first picture present a milky matte color in the second show a watery red brown with a few minutes of difference.



Figure 4.18: New Chitosan/350 °C sample (left) prepared in compare with an old Chitosan/350 °C sample (right)

In Fig. 4.18, two solutions of [chitosan/350° C] samples prepared 16 days apart using the same procedure were observed. The sample on the left was prepared minutes before taking the photo, while the sample on the right was prepared

16 days ago. The sample on the left, which has already been explained, shows a matte color similar to a brick. On the other hand, the sample on the right shows a dark brown color with green flashes on the surface. One hypothesis that can explain this phenomenon is the natural oxidation of copper, which presents this coloration under environmental conditions<sup>32-34</sup>. When the sample prepared 16 days ago was used for film preparation, it did not emit any signal. This feature could be attributed to a short useful life<sup>35,36</sup>.

#### 4.4 DAQ "NI USB-6210" Circuit

The homemade circuit based in DAQ "NI USB-6210" model was employed in conjunction with a white light LED lantern to analyzed the photoconductance in the chitosan copper oxide films previously elaborated over the interdigitates see in Fig.3.2(b). For the first measure were elaborated 6 samples of each calcinated sample with a 5% of NPs.

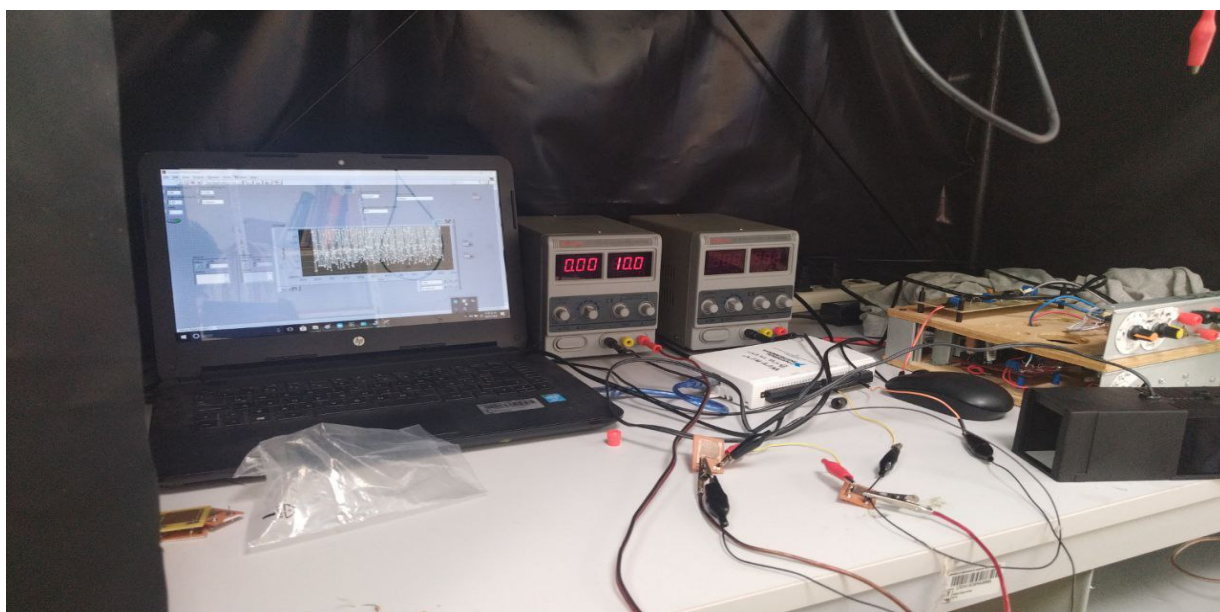


Figure 4.19: DAQ "NI USB-6210" Circuit Set Up

On this first measure, any of the samples present a signal that can be recorded in the circuit. Some explanations for this can be the limited useful life of interdigitates or an inefficient metallic NPs percentage present in the film. To avoid these factors a second batch of interdigitates with 5% of NPs were elaborated and measure instantly to be fabricated. The reason for connecting two interdigitated structures in series, despite increasing the total resistance and lowering the conductance, lies in the voltage divider effect. When connected in series, the applied voltage is divided between the two structures in proportion to their resistances. This allows for finer control over the voltage drop across each structure, enabling the study of how each one behaves under different voltage conditions. Although this configuration increases resistance, it provides a tool for manipulating the electric field distribution and the overall electronic properties of the system. The result was that [Chitosan/600 °C] at 5% sample present a little signal in the circuit until [Chitosan/350 °C] samples not. For a second measure were employed a new batch of interdigitates with 1% of metallic NPs that were prepared the same day. In this case [Chitosan/600 °C] samples present a signal that can be recorded showed in Fig.4.22 while [Chitosan/350°C] samples not present any signal.

Finally, a third batch was elaborated employing 2.5% of NPs of each sample and measure in DAQ circuit. [Chitosan/600 °C] samples were the only that present signals but not to notable as samples at 1%. For that reason the next measures were only in interdigitates of [Chitosan/600 °C] at 1% samples. For the second part of the experiment were employed three



different light filters to determine how spectrum could affect to photoconductance of the samples. Fig.4.22 was consider as control sample for the next results. White light sample give us a behavior similar to a capacitor with an average amplitude of  $0.075 \mu A$  to belong the measure. In Fig.4.20 was possible to appreciate a typically behavior exhibits by a commercial capacitor in charging and discharging cycles, producing an oscillating current with decreasing amplitude as the system reaches equilibrium. The criteria used for this determination are based on the regularity of the current oscillations and their decreasing amplitude over time. This behavior aligns with the exponential decay pattern of current in a discharging capacitor. The steady response under white light, and its sensitivity to changes in external stimuli (such as light intensity), further supports the hypothesis that the sample behaves in a capacitive manner. To obtain the average current, in Google Colab the results of DAQ circuit were analyzed with scipy package to find the peaks and valleys to determine the amplitude of each cycle, these results were saved in a DataFrame with pandas package and averaged by numpy package.

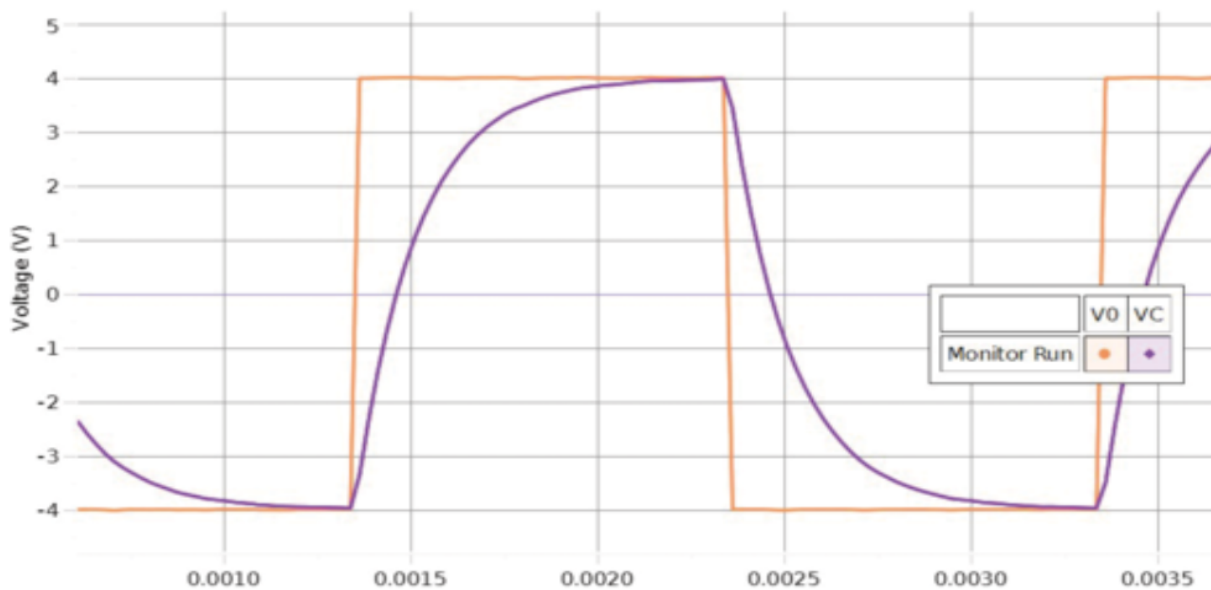


Figure 4.20: RC Series Circuit showing the charge and discharge behavior of a capacitor. The graph illustrates the voltage across the capacitor (VC) and the input voltage (V0) over time. Recover from (PASCO Scientific, 2024)

The light filters employed in the analysis were red, blue, and green, obtaining the spectrum shown in Fig.4.24. Each filter was analyzed with commercial spectroscopy to determine the affected zones in the visible spectrum. To ensure accuracy, each filter was tested three times, and the best reading was selected for this research. For the red filter, two principal peaks were observed around 440 and 589 nm. These peaks correspond to the following color ranges: violet (380-450 nm), blue (450-495 nm), green (495-570 nm), yellow (570-590 nm), orange (590-620 nm), and red (620-750 nm). The zones with the least interference were from blue to green and from orange onwards. The blue filter showed principal peaks at 445 and 509 nm, covering the violet to green range while allowing the rest of the light spectrum to pass. The green filter had principal peaks at 451, 523, and 577 nm, corresponding to the blue to orange range in the spectrum. The use of these filters is crucial to understanding how different wavelengths of light influence the film, which has band gaps of 2.331 eV and 1.248 eV (see Fig. 4.13 and Fig.4.14). Each filter isolates specific ranges of the visible spectrum, allowing for the analysis of the material's spectral sensitivity. This helps determine how the photoconductive behavior varies under different wavelengths, which is an important factor for optimizing the material's performance in optoelectronic applications.

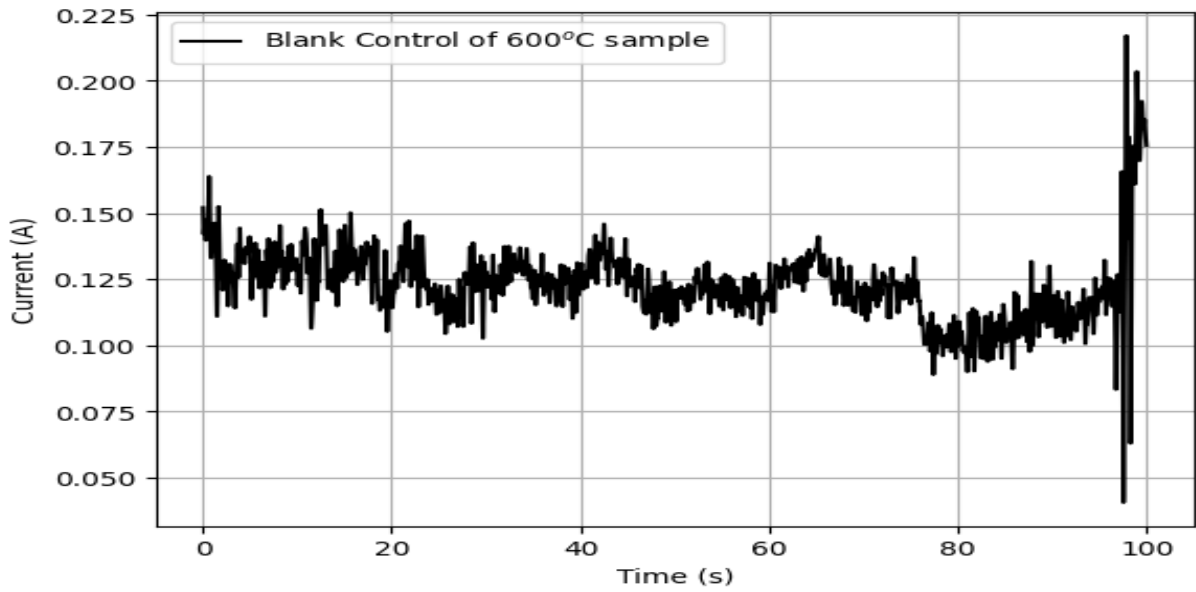


Figure 4.21: Blank Control recover from [Chitosan/600°C] sample at 1% NPs, recorded using the DAQ 'NI USB-6210' Circuit.

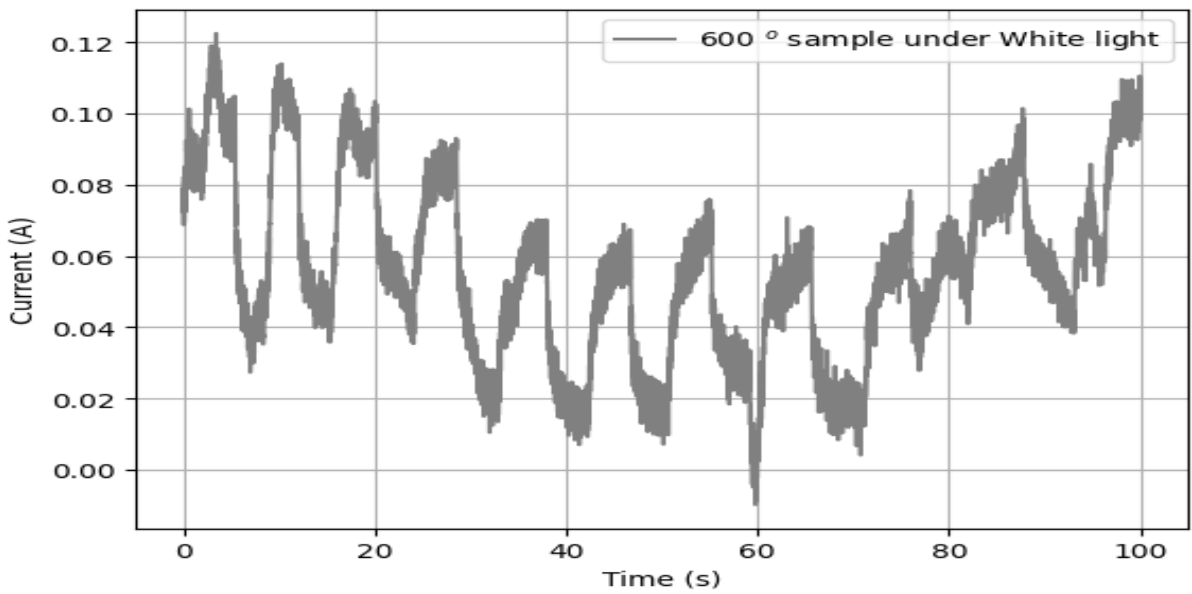


Figure 4.22: Current measurement of the [Chitosan/600°C] sample at 1% NPs, recorded using the DAQ 'NI USB-6210' Circuit. This graph illustrates the photoconductive behavior under white light exposure, showing a stable response similar to a capacitor with an average amplitude of  $0.075 \mu\text{A}$ .

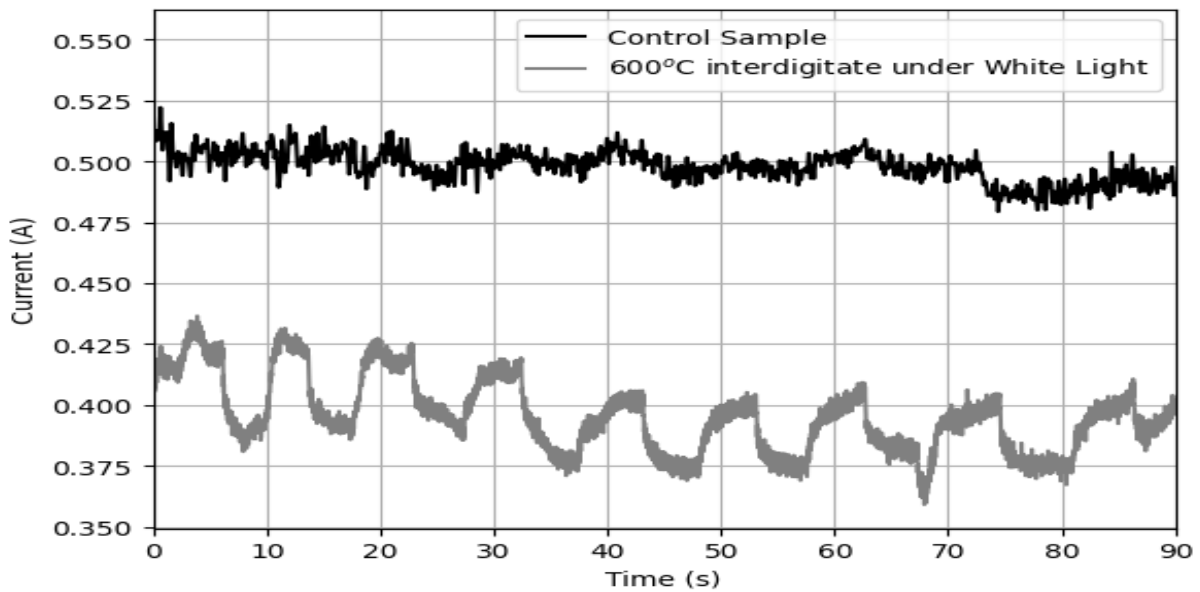


Figure 4.23: Compare between control measure and white light measure of 600 °C at 1% NPs concentration interdigitate.

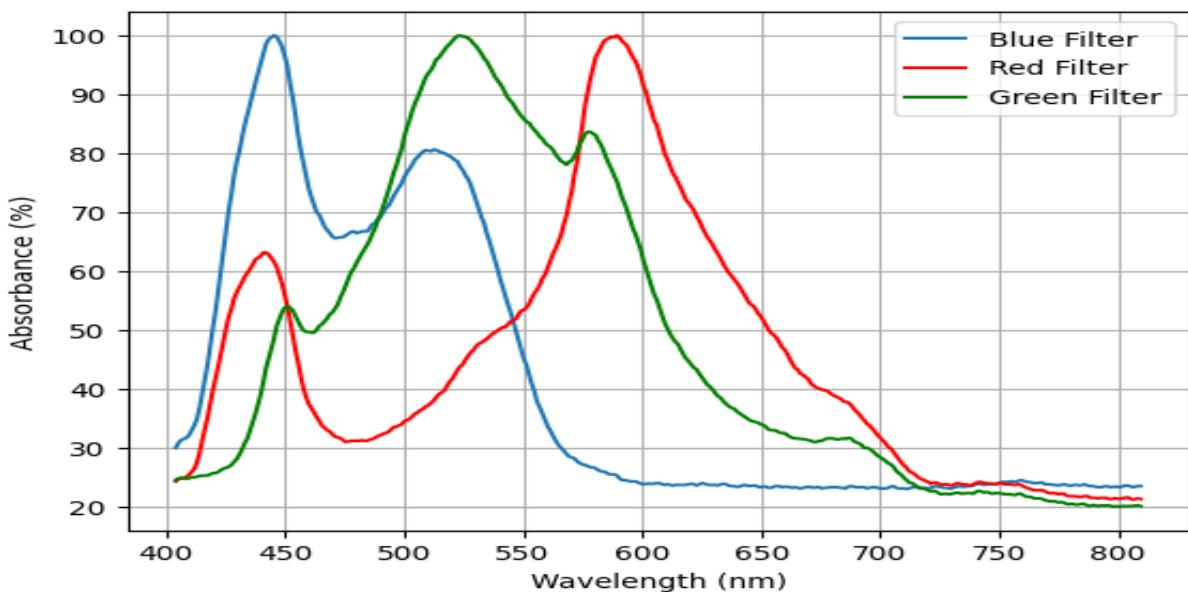
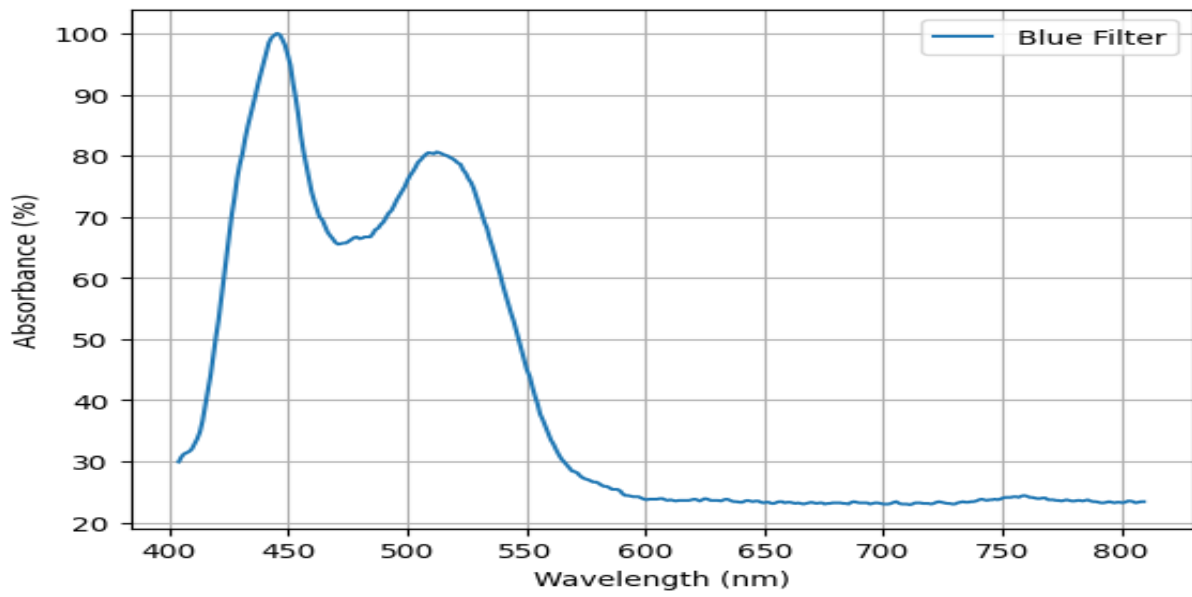
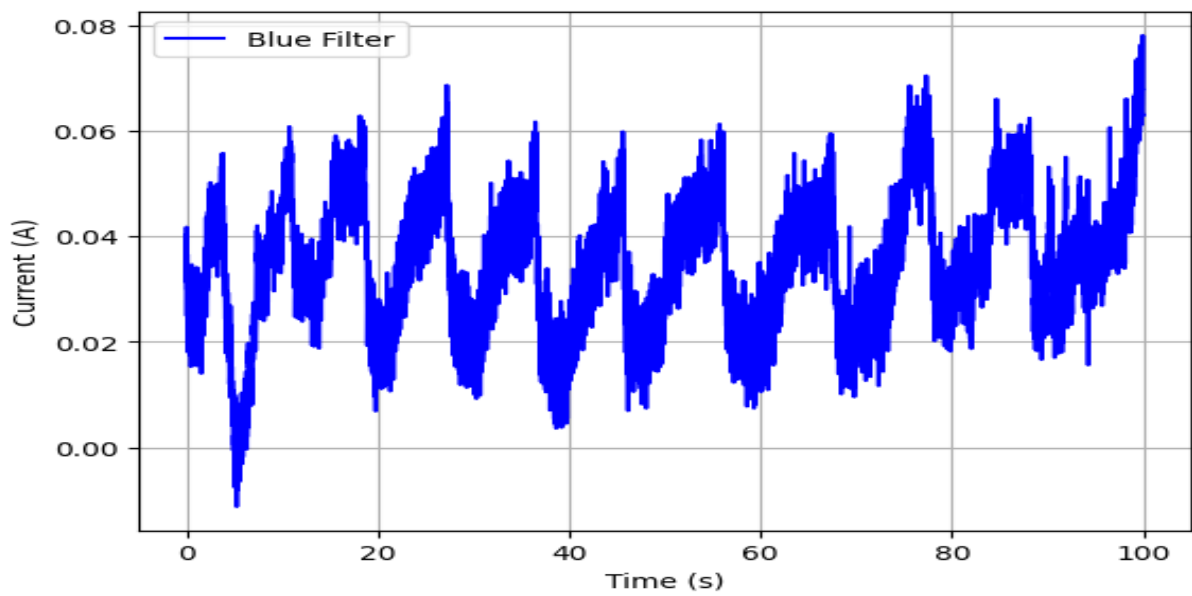


Figure 4.24: Light Filters spectrums employed in analysis in photoconductance of [Chitosan/600 °C] at 1% NPs.

For the blue filter, the average amplitude current measure was  $0.0375 \mu A$ . In compare with the amplitude obtained in control measure we notice a reduction to the half. Their peaks and valleys are more flat than the control, if we consider that 600 °C calcinated sample present a band gap of 2.331 eV equivalent to 531.96 nm and that blue filter are present in a range of 400 to 550 nm approx (belonging to violet to green range). In base on this information, we can affirm that  $Cu_2O$  NPs present in the sample play a considerable roll in the photoconductance behavior of the film. This can be confirmed later when the green filter was analyzed. Fig.4.25(b) shows the same tendency to be similar to a capacitor to a notable consistency between cycles to turn on and turn of the light source.



(a) Blue filter spectrum



(b) Current measure under the blue filter

Figure 4.25: Interdigitate under a blue light filter current measure

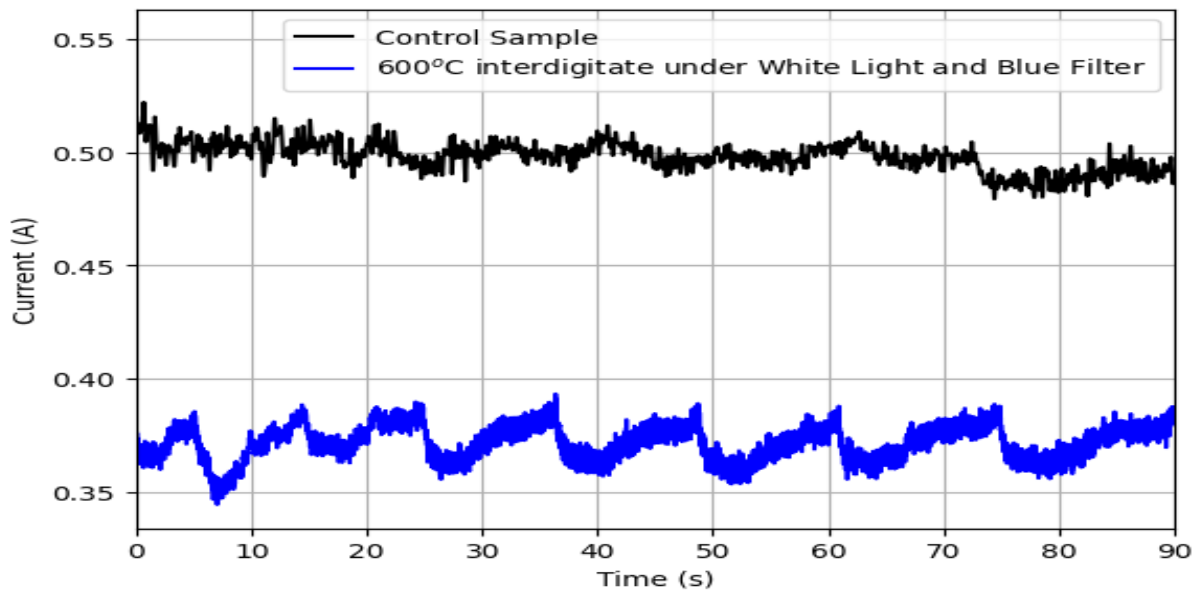


Figure 4.26: Compare between a control measure and blue filter measure.

For the green light filter the average amplitude current measure was  $0.0365 \mu A$ . This value is technically the same watched in the blue light filter. According to the spectrum of the green filter, the range that are be affected by the filter was from 445 to 650 nm that correspond to violet to orange range. The reduction to the half again can be attributed to the presence of  $Cu_2O$  in the 600 °C calcinated sample. Similar behavior and tendency of blue filter.

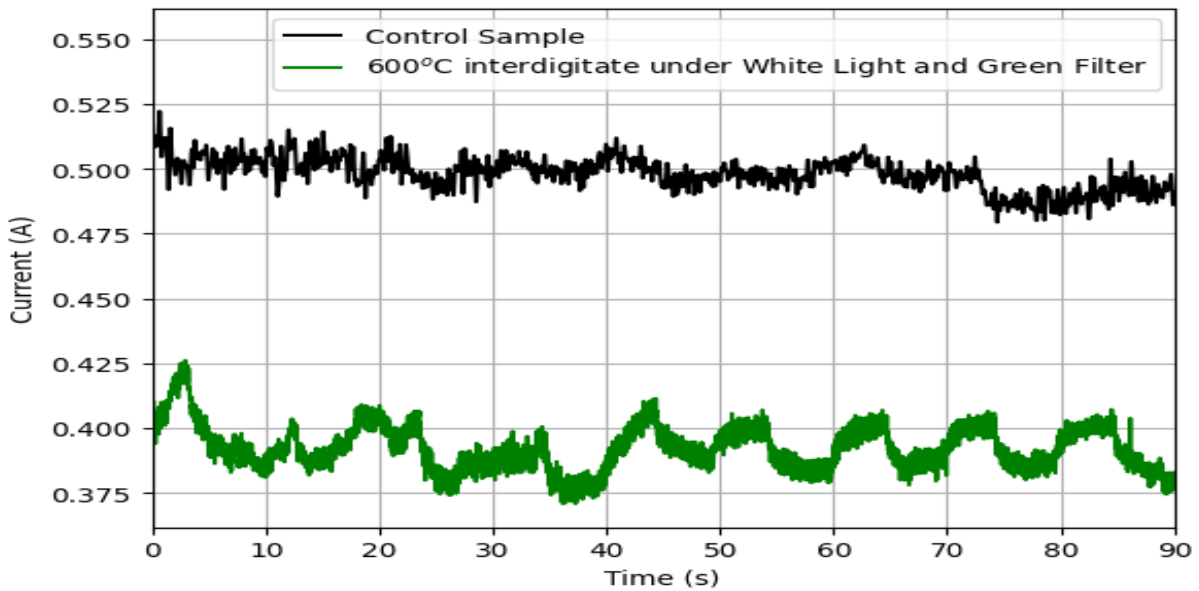
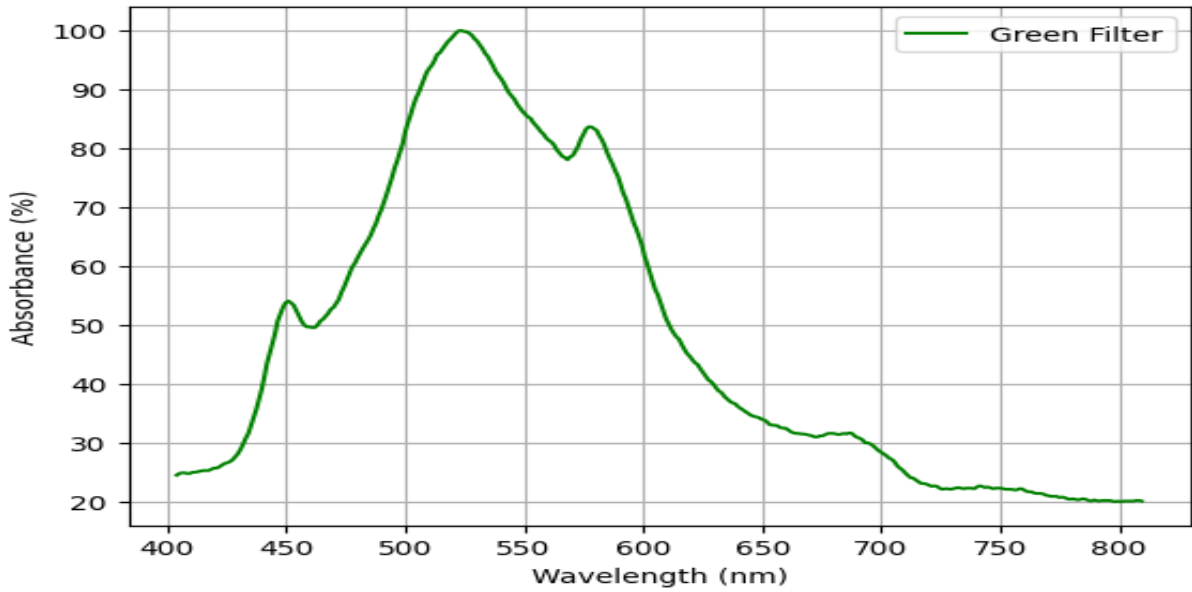
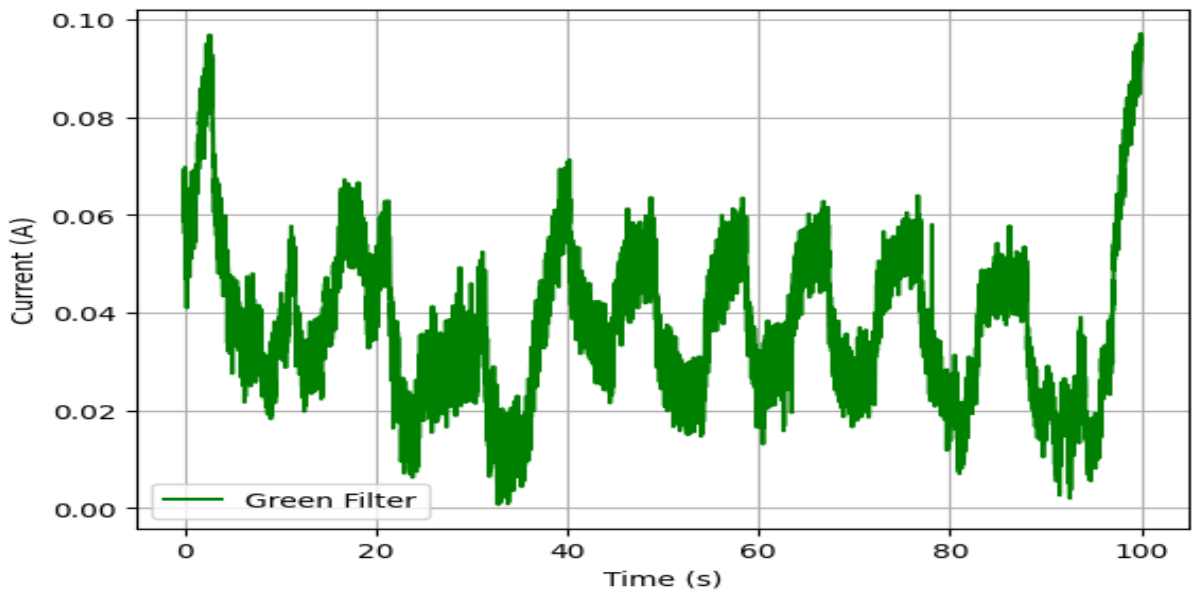


Figure 4.27: Compare between a control measure and green filter measure.



(a) Green filter spectrum

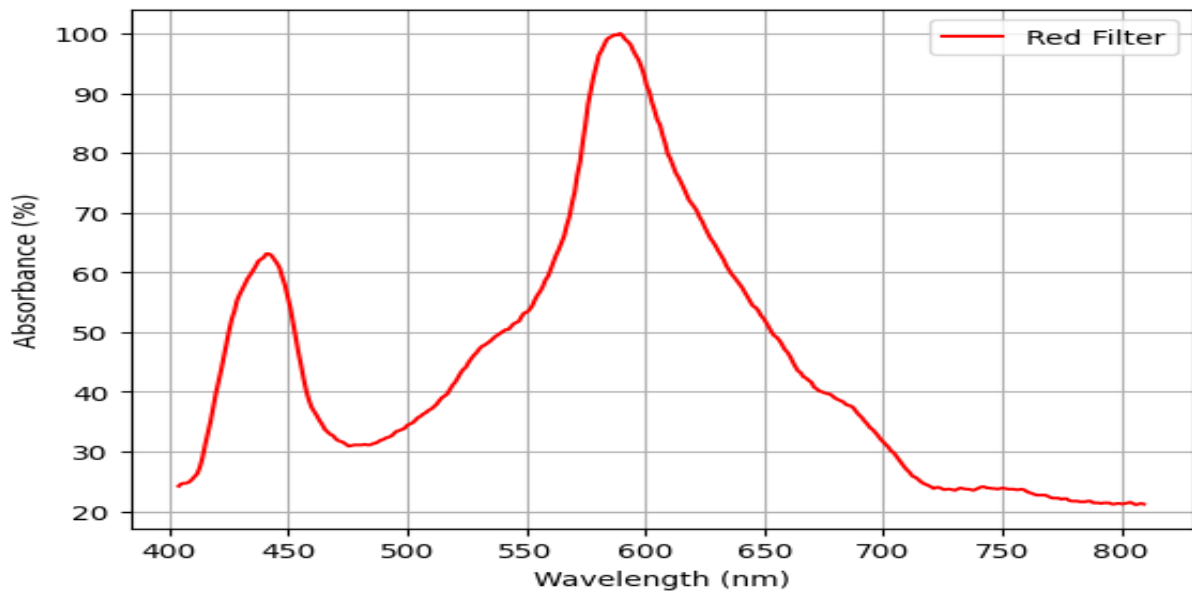


(b) Current measure under the green filter

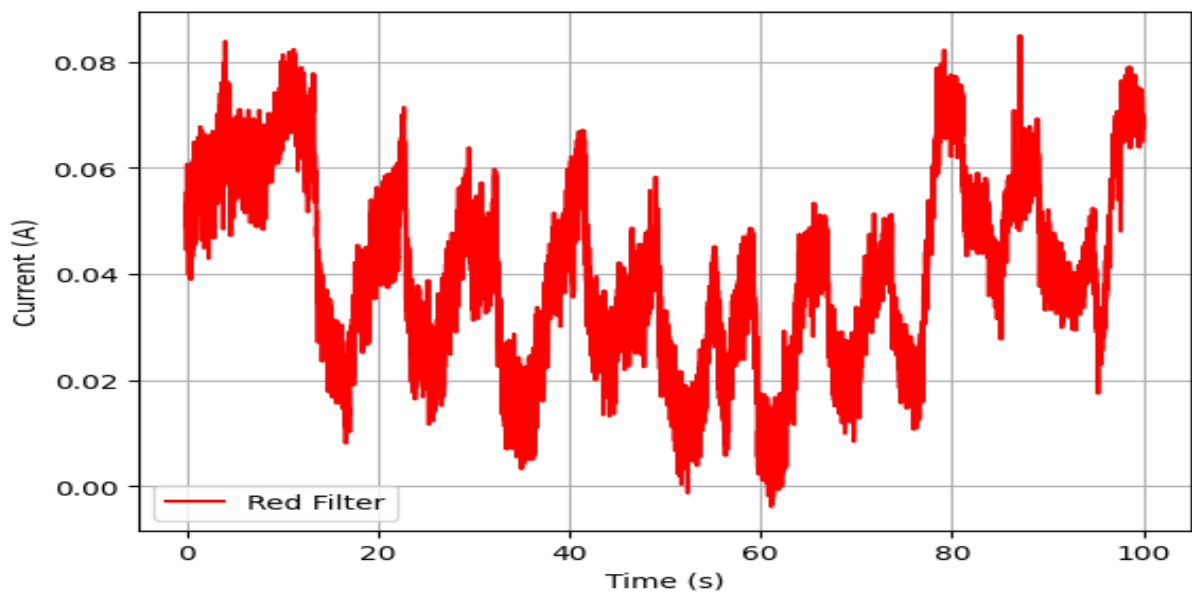
Figure 4.28: Interdigitate under a green light filter current measure

For the red light filter the average amplitude current measure was  $0.086 \mu A$ . In this case, red light filter interfere considerable in two range, from 400 to 450 nm and 530 to 680 nm. In compare with the control and the previous filters, red light filter present a better photoconductance behavior. On the other hand, its tendency continuously be similar to a capacitor but with an erratic behavior. In this case it is necessary to denote that band gap of  $Cu_2O$  be benefited if it is not in contact with the rest of visible spectrum. The improved photoconductance with the red filter can be explained by the material's higher sensitivity to red light, which allows specific wavelengths (620–750 nm) to pass through while blocking others. This reduces interference from other wavelengths, allowing for more efficient photoconductive behavior. Additionally, the red photons may better match the energy of the material's band gap, leading to increased absorption and

the generation of more charge carriers. By isolating the optimal wavelengths, the red filter enhances photoconductance compared to unfiltered light.



(a) Red filter spectrum



(b) Current measure under the red filter

Figure 4.29: Interdigitate under a red light filter current measure

Finally, due to the lack of an infrared light source, the contribution of  $CuO$  in the film cannot be directly analyzed. However, it can be hypothesized that  $CuO$  plays a role in the photoconductive behavior of the film, as both the blue and green filters show similar current measurements. This is despite the interference being located within the band gap of  $Cu_2O$ , suggesting that  $CuO$  could be contributing to the overall response of the film.

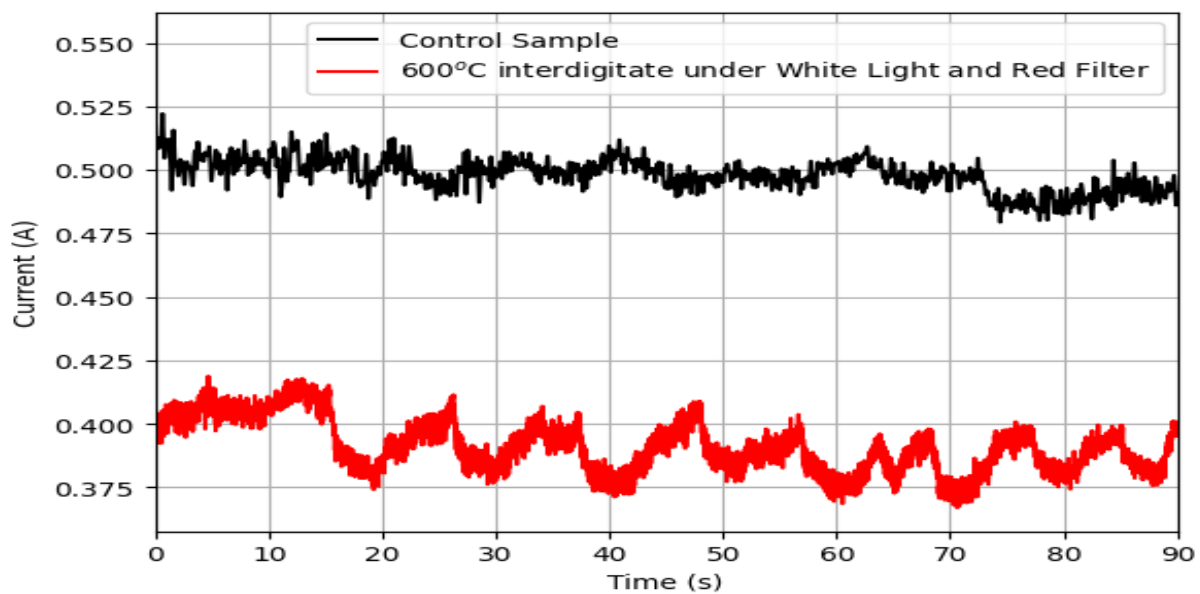


Figure 4.30: Compare between control measure and red filter



## Chapter 5

# Conclusions

The oxidation of copper oxide nanoparticles significantly influences the photoconductance results. It is essential to minimize the time between synthesis and current measurement to avoid variations in material properties, which aligns with the objective of optimizing the manufacturing process and ensuring quality control.

The copper oxide films in a chitosan matrix exhibit limitations in their useful life due to susceptibility to oxidation, which suggests exploring other, more stable polymers. This finding supports the objective of evaluating the viability of materials for sustainable applications and indicates the need for future research in alternative polymers.

Results show that calcination at 600 °C promotes the formation of  $CuO$ , improving photoconductance compared to calcination at 350 °C. This finding contributes to the objective of understanding how thermal treatments impact the properties of the materials, particularly in terms of enhancing photoconductance.

Photoconductance analysis with light filters reveals that  $Cu_2O$  and  $CuO$  show distinct responses under red, blue, and green light. This result validates the objective of studying the response to different wavelengths and reinforces the potential application in optoelectronic devices.

Copper oxide-based photoconductance devices show potential for replacing traditional devices, provided current limitations are addressed. This finding aligns with the overall thesis objective of exploring new materials for optoelectronic applications and suggests a clear direction for future research and applications.



# Bibliography

- [1] WSTS, Semiconductor Industry BLUE BOOK HISTORY. 2023; <https://www.wsts.org/61/MARKET-STATISTICS>.
- [2] Vimala Rani, M.; Mathirajan, M. A state-of-art review and a simple meta-analysis on deterministic scheduling of diffusion furnaces in semiconductor manufacturing. *International Journal of Production Research* **2023**, *61*, 5744–5771.
- [3] others,, *et al.* Review on the processing and properties of polymer nanocomposites and nanocoatings and their applications in the packaging, automotive and solar energy fields. *Nanomaterials* **2017**, *7*, 74.
- [4] Singh, J.; Kaur, G.; Rawat, M. A brief review on synthesis and characterization of copper oxide nanoparticles and its applications. *J. Bioelectron. Nanotechnol* **2016**, *1*.
- [5] Chang, X. X.; Mubarak, N. M.; Mazari, S. A.; Jatoi, A. S.; Ahmad, A.; Khalid, M.; Walvekar, R.; Abdullah, E.; Karri, R. R.; Siddiqui, M. A review on the properties and applications of chitosan, cellulose and deep eutectic solvent in green chemistry. *Journal of industrial and engineering chemistry* **2021**, *104*, 362–380.
- [6] Sawant, S. S.; Bhagwat, A. D.; Mahajan, C. M. Synthesis of cuprous oxide (Cu<sub>2</sub>O) nanoparticles—a review. - **2016**, 01035–1.
- [7] Ighalo, J. O.; Sagboye, P. A.; Umenweke, G.; Ajala, O. J.; Omoarukhe, F. O.; Adeyanju, C. A.; Ogguniyi, S.; Adeniyi, A. G. CuO nanoparticles (CuO NPs) for water treatment: A review of recent advances. *Environmental Nanotechnology, Monitoring & Management* **2021**, *15*, 100443.
- [8] El-Trass, A.; ElShamy, H.; El-Mehasseb, I.; El-Kemary, M. CuO nanoparticles: synthesis, characterization, optical properties and interaction with amino acids. *Applied Surface Science* **2012**, *258*, 2997–3001.
- [9] Nine, M. J.; Munkhbayar, B.; Rahman, M. S.; Chung, H.; Jeong, H. Highly productive synthesis process of well dispersed Cu<sub>2</sub>O and Cu/Cu<sub>2</sub>O nanoparticles and its thermal characterization. *Materials Chemistry and Physics* **2013**, *141*, 636–642.
- [10] Li, S.; Meng, L.; Toprak, M.; Kim, D. K.; Muhammed, M. Nanocomposites of Polymer and Inorganic Nanoparticles for Optical and Magnetic Applications. *Nano reviews* **2010**, *1*.
- [11] Kucherov, A.; Kramareva, N.; Finashina, E.; Koklin, A.; Kustov, L. Heterogenized redox catalysts on the basis of the chitosan matrix: 1. Copper complexes. *Journal of Molecular Catalysis A: Chemical* **2003**, *198*, 377–389.
- [12] Sze, S. M.; Ng, K. K. *Physics of Semiconductor Devices*, 3rd ed.; Wiley-Interscience, 2006.
- [13] Pierret, R. F. *Semiconductor Device Fundamentals*; Addison-Wesley, 1996.

- [14] Yacobi, B. G. *Semiconductor materials: an introduction to basic principles*; Springer Science & Business Media, 2003.
- [15] Terna, A. D.; Elemike, E. E.; Mbonu, J. I.; Osafire, O. E.; Ezeani, R. O. The future of semiconductor nanoparticles: Synthesis, properties and applications. *Materials Science and Engineering: B* **2021**, *272*, 115363.
- [16] Chen, W. *The Microelectronics Race: The Impact of Government Policy on International Competition*; Springer, 2006.
- [17] Patel, M.; Patel, M.; Dadhaniya, P.; Vora, J.; Soni, S. Eco-friendly synthesis of copper oxide nanoparticles using leaf extract of plant *Moringa oleifera* and their potential applications as antibacterial agents. *Materials Science and Engineering: C* **2020**, *116*, 111254.
- [18] Bansal, V.; Sharma, P. K.; Sharma, N.; Pal, O. N.; Malhotra, B. D. Prospects of nanostructure materials and their composites as antimicrobial agents. *Journal of Materials Chemistry B* **2015**, *3*, 416–433.
- [19] Kumar, A.; Neeraj, Green synthesis of copper oxide nanoparticles using Aloe vera leaf extract and its antibacterial activity. *Journal of Microbiology, Biotechnology and Food Sciences* **2018**, *7*, 317–320.
- [20] Nithya, A.; Jothivenkatachalam, K.; Prabhu, S.; Jeganathan, K. Chitosan based nanocomposite materials as photocatalyst—a review. 2014.
- [21] Jian-peng, D.; Hang, L.; Xiao-Ling, P.; Chao-Ni, Z.; Tian-Huai, Y.; Xian-Min, J. Research progress of quantum memory. *Acta Physica Sinica* **2019**,
- [22] Shi, J.; Zhang, J.; Yang, L.; Qu, M.; Qi, D.-C.; Zhang, K. H. Wide bandgap oxide semiconductors: from materials physics to optoelectronic devices. *Advanced materials* **2021**, *33*, 2006230.
- [23] Chen, W.; Zhang, J. Z.; Joly, A. G. Optical properties and potential applications of doped semiconductor nanoparticles. *Journal of nanoscience and nanotechnology* **2004**, *4*, 919–947.
- [24] Biju, V.; Itoh, T.; Anas, A.; Sujith, A.; Ishikawa, M. Semiconductor quantum dots and metal nanoparticles: syntheses, optical properties, and biological applications. *Analytical and bioanalytical chemistry* **2008**, *391*, 2469–2495.
- [25] Khan, A.; Rashid, A.; Younas, R.; Chong, R. A chemical reduction approach to the synthesis of copper nanoparticles. *International Nano Letters* **2016**, *6*, 21–26.
- [26] Khan, A.; Rashid, A.; Younas, R.; Chong, R. A chemical reduction approach to the synthesis of copper nanoparticles. *International Nano Letters* **2016**, *6*, 21–26.
- [27] El-Trass, A.; ElShamy, H.; El-Mehasseb, I.; El-Kemary, M. CuO nanoparticles: synthesis, characterization, optical properties and interaction with amino acids. *Applied Surface Science* **2012**, *258*, 2997–3001.
- [28] Nine, M. J.; Munkhbayar, B.; Rahman, M. S.; Chung, H.; Jeong, H. Highly productive synthesis process of well dispersed Cu<sub>2</sub>O and Cu/Cu<sub>2</sub>O nanoparticles and its thermal characterization. *Materials Chemistry and Physics* **2013**, *141*, 636–642.
- [29] Cullity, B. D.; Stock, S. R. *Elements of X-ray Diffraction*, 3rd ed.; Prentice-Hall: Upper Saddle River, New Jersey, 1978; pp 170–174, Scherrer Equation for X-ray diffraction analysis.
- [30] Zayed, M. F.; Eisa, W. H.; Abd ElHameed, M. H.; Abou Zeid, A. M. Spectroscopic investigation of chitosan-supported Cu<sub>2</sub>O/CuO nanocomposite; a separable catalyst for water-pollutants degradation. *Journal of Alloys and Compounds* **2020**, *835*, 155306.

- [31] Markus Heinemann, C. H., Bianca Eifert Band Structure and Phase Stability of the Copper Oxide System. *Physical Review B* **2013**, *87*, 115111.
- [32] Ltaief, S.; Jabli, M.; Ben Abdesslem, S. Immobilization of copper oxide nanoparticles onto chitosan biopolymer: Application to the oxidative degradation of Naphthol blue black. *Carbohydrate Polymers* **2021**, *261*, 117908.
- [33] Mekonnen, E. G.; Shitaw, K. N.; Hwang, B.-J.; Workie, Y. A.; Abda, E. M.; Mekonnen, M. Copper nanoparticles embedded fungal chitosan as a rational and sustainable bionanozyme with robust laccase activity for catalytic oxidation of phenolic pollutants. *RSC Advances* **2023**, *13*, 32126–32136.
- [34] Rathore, B. S.; Chauhan, N.; Rawal, M. K.; Ameta, S. Chitosan–polyaniline–copper(II) oxide hybrid composite for the removal of methyl orange dye. *Polymer Bulletin* **2019**, *77*, 4833–4850.
- [35] Chetia, M.; Ali, A. A.; Bhuyan, D.; Saikia, L.; Sarma, D. Magnetically recoverable chitosan-stabilised copper–iron oxide nanocomposite material as an efficient heterogeneous catalyst for azide–alkyne cycloaddition reactions. *New Journal of Chemistry* **2015**, *39*, 5902–5907.
- [36] Chang, Y.; Wang, Y.; Zha, F.; Wang, R. Preparation and catalytic properties of chitosan bound Schiff base copper complexes. *Polymers for Advanced Technologies* **2004**, *15*, 284–286.



# Appendices





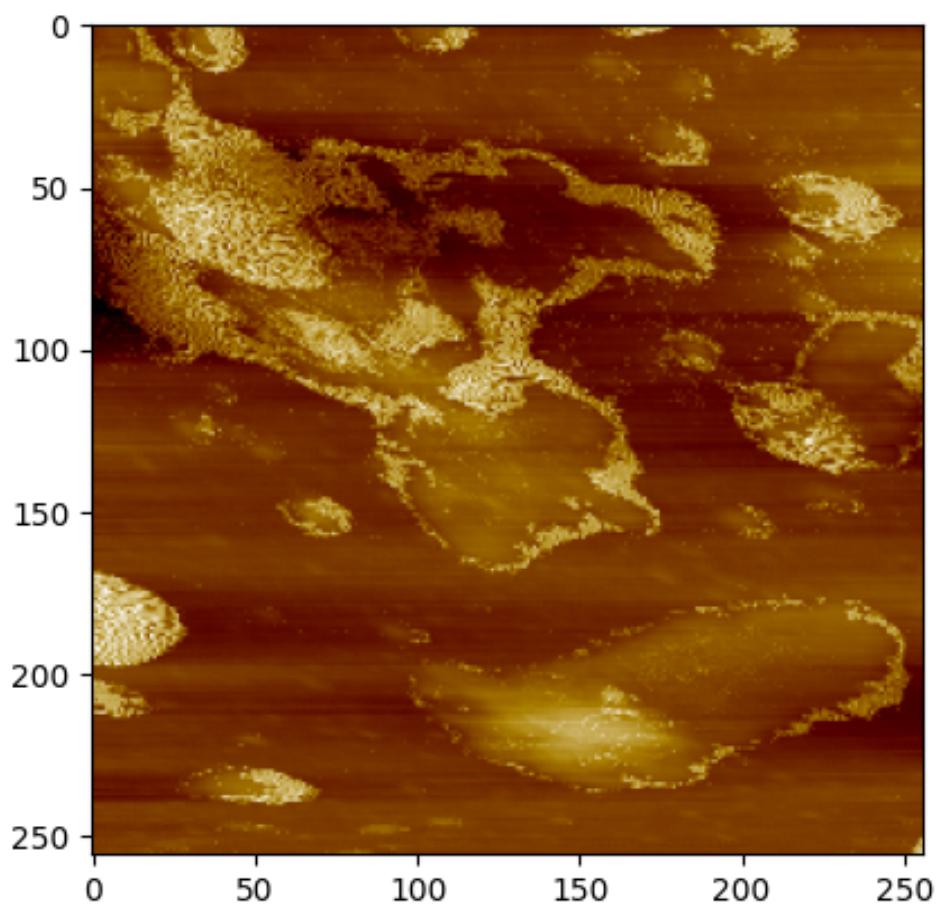


Figure 1: AFM height forward measure of first synthesis of metallic copper oxide NPs